

A Unified Phase-Field Fourier Neural Network Framework for Topology Optimization

Jing Li* Xindi Hu[†] Helin Gong[‡] Wei Gong[§] Shengfeng Zhu[¶]

November 19, 2025

Abstract

This paper presents a unified and physics-driven framework of alternating phase-field Fourier neural networks (APF-FNNs) for topology optimization. At its core, an alternating architecture decouples the optimization by parameterizing the state, adjoint and topology fields with three distinct Fourier Neural Networks (FNNs). These networks are trained through a collaborative and stable alternating optimization scheme applicable to both self-adjoint and non-self-adjoint systems. The Ginzburg-Landau energy functional is incorporated into the topology network’s loss function, acting as an intrinsic regularizer that promotes well-defined designs with smooth and distinct interfaces. By employing physics-informed losses derived from either variational principles or strong-form PDE residuals, the broad applicability of the APF-FNNs is demonstrated across a spectrum of 2D and 3D multi-physics benchmarks, including compliance minimization, eigenvalue maximization, and Stokes/Navier-Stokes flow optimization. The proposed APF-FNNs consistently yield high-performance and high-resolution topologies, establishing a powerful and versatile foundation for physics-driven computational design.

Keywords: Topology Optimization; Phase-Field Method; Fourier Neural Networks; Alternating Optimization; Physics-Driven Neural Networks.

Mathematical Subject Classification: 49Q10, 49M41, 68T07, 35Q93

1 Introduction

Topology optimization (TO) has emerged as a transformative computational paradigm in engineering design, enabling the optimal material distributions within a given domain to maximize performance under specified loads and boundary conditions [1–3]. By exploring a vast design space, TO produces high-performance topologies that often surpass conventional and experience-based designs. This capability has driven remarkable progress in developing lightweight and efficient components across diverse engineering fields [4, 5], establishing TO as a cornerstone of modern computational design. Its impact has been further amplified by additive manufacturing [6, 7], which enables the realization of intricate, performance-driven topologies, fostering a powerful synergy that continues to advance engineering innovation.

*School of Mathematical Sciences, East China Normal University, Shanghai 200241, China. (betterljing@163.com)

[†]Department of Applied Mathematics, The Hong Kong Polytechnic University, Kowloon, Hong Kong, China (xindi.hu@polyu.edu.hk)

[‡]Paris Elite Institute of Technology, Shanghai Jiao Tong University, Shanghai 200240, China. (gonghelin@sjtu.edu.cn)

[§]NCMIS&SKLMS, Institute of Computational Mathematics and Scientific/Engineering Computing, Academy of Mathematics and Systems Science, Chinese Academy of Sciences, Beijing, China. (wgong@lsec.cc.ac.cn)

[¶]Corresponding author. Key Laboratory of Mathematics and Engineering Applications & Shanghai Key Laboratory of Pure Mathematics and Mathematical Practice, East China Normal University, Shanghai 200241, China. (sfzhu@math.ecnu.edu.cn)

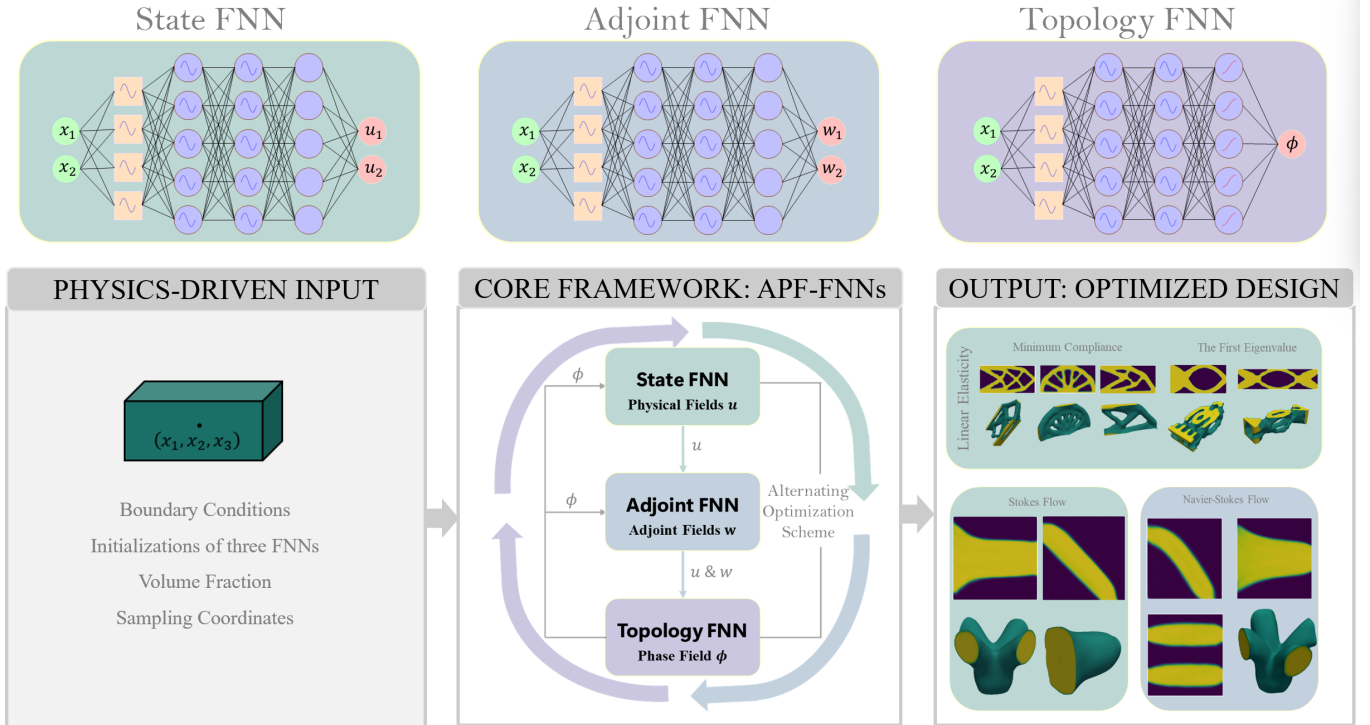


Figure 1: **Schematic overview of the Alternating Phase-Field Fourier Neural Networks (APF-FNNs)**. The process begins with the physics settings (left panel). The core framework (middle panel) features an alternating architecture with three distinct FNNs parameterizing the state u , adjoint w and topology ϕ fields. These networks are trained collaboratively through a stable alternating optimization scheme. The versatility of the framework (right panel) is demonstrated by solving a range of benchmark problems, encompassing both self-adjoint (e.g., linear elasticity and Stokes flow) and non-self-adjoint (e.g., Navier-Stokes flow) systems.

Originating from the seminal homogenization method [8], the practical implementation of topology optimization [9] has been dominated by mesh-based paradigms like the Solid Isotropic Material with Penalization method [10,11] and Bi-directional Evolutionary Structural Optimization [12]. Despite their widespread application, these approaches are plagued by numerical pathologies such as checkerboard patterns, mesh-dependency, and unresolved intermediate densities [13,14]. These issues are symptomatic of a fundamental ill-posedness inherent in the TO problem formulation. Consequently, achieving manufacturable designs has relied on ad-hoc remedies like density filtering or projection to impose a minimum length scale [15,16]. To overcome these limitations, more fundamental approaches decouple the geometric representation from the analysis mesh. While the level-set method excels at producing crisp, well-defined boundaries, its design exploration is fundamentally constrained by its inability to nucleate new holes within the domain [3,17,18]. The phase-field method has emerged as a particularly compelling alternative, effectively circumventing the limitations of both prior approaches [19–22]. Grounded in the variational principles of phase transition physics, the phase-field framework not only accommodates complex topological changes like hole nucleation and member merging inherently, but its intrinsic Ginzburg-Landau energy functional also provides physical regularization [23–25]. This dual capability ensures a well-posed problem and suppresses numerical artifacts without resorting to the heuristic schemes required by traditional mesh-based methods [26].

However, despite its conceptual advantages, conventional phase-field TO is hindered by significant

computational challenges. The primary issue is the substantial cost of accurately solving the governing partial differential equations (PDEs), namely the state equation and the phase-field evolution equation (e.g., the Allen-Cahn or Cahn-Hilliard equation [27, 28]). Within the Finite Element Method (FEM) framework, this process demands numerous iterations to solve large and nonlinear systems of equations at each optimization step [29]. Furthermore, a critical bottleneck arises from the coupling of geometry and discretization within FEM: sharpness of the material interface is directly tied to the mesh resolution, as the diffuse interface must be resolved by several elements for numerical stability [24]. Consequently, achieving a high-resolution design with crisp boundaries necessitates a globally dense mesh. This dual demand for iterative solutions on fine meshes renders the entire procedure computationally prohibitive for high-resolution 2D and most 3D problems [30], severely restricting the application in large-scale engineering design and necessitating the search for more efficient solution approaches.

Deep neural networks have emerged as powerful and mesh-free function approximators for solving PDEs, driving a paradigm shift in scientific computing [31–36]. They offer the potential to mitigate the curse of dimensionality and handle complex geometries more flexibly than traditional methods. Among these, two leading frameworks are the Physics-Informed Neural Networks (PINNs) [32] and the Deep Ritz Method (DRM) [33]. While PINNs offer broad versatility by embedding strong-form PDE residuals into the loss function, enabling their application to any system of equations, even those without a known variational principle, DRM is tailored for problems with a variational structure, minimizing the system’s energy functional, which is advantageous for stability and handling natural boundary conditions. Leveraging this fundamental distinction, a hybrid strategy strategically employs PINNs for non-variational state equations, while reserving DRM for those possessing an energy functional. The variational nature of the phase-field model renders the DRM an ideally suited approach for the TO objective.

Early studies of NNs in TO are predominantly data-driven, treating the problem as image-to-image translation or generative design [37–43]. The first wave of research employs surrogate models to learn a direct mapping from problem conditions to a final topology, thereby bypassing expensive iterative solvers [40]. More recent approaches leverage generative models, such as GANs, to explore the design space from a latent representation and impose complex and non-differentiable manufacturing constraints [44–46]. Despite their promise, a fundamental limitation plagues these purely data-driven paradigms: their reliance on vast datasets of pre-computed designs. This dependency biases the models towards replicating visual features rather than adhering to physical principles, often resulting in mechanically unsound or disconnected topologies. Consequently, their performance is inherently capped by the scope of the training data, severely compromising their generalizability and reliability for engineering applications.

Initial physics-informed strategies addressed the limitations of purely data-driven models by reparameterizing the design field with neural networks [47, 48]. This reshaped the optimization landscape but still relied on finite element solvers for physical analysis. Subsequent developments, such as energy-based PINNs, replaced FEM by solving state fields without labeled data [49, 50], although the design optimization remained dependent on conventional schemes. Alternatively, mesh-free approaches with dual-network architectures have emerged, employing two coupled neural networks, a density network for the material layout and a physics network for the corresponding state fields [51, 52]. A unified and energy-based loss derived from variational principles couples the two networks, enabling simultaneous, end-to-end optimization of topology and physical response while eliminating the need for finite element analysis and analytical sensitivity calculations. Current approaches either combine all physical and design objectives into a single monolithic loss [53], often producing a complex optimization landscape with difficult penalty balancing and unstable training, or rely on formulations restricted to specific objectives, such as linear elastic compliance in multi-material phase-field design [54], limiting broader applicability. These limitations highlight the need for a framework that is general and capable of handling both self-adjoint and non-self-adjoint systems, and structured to ensure stable and robust optimization.

The primary contributions of the proposed **Alternating Phase-Field Fourier Neural Networks (APF-FNNs)** as shown in Fig. 1 include the following:

- **A decoupled multi-FNN architecture:** In contrast to coupled approaches, APF-FNNs decouple the problem by employing three distinct FNNs to independently parameterize the state, adjoint and topology fields. This architecture leverages the superior parameter efficiency of FNNs in representing complex functions. By overcoming the spectral bias of traditional Multi-Layer Perceptrons (MLPs), FNNs can capture fine, high-frequency details without a prohibitive increase in network size, ensuring both representational power and computational feasibility.
- **Robust alternating optimization for broad applicability:** The alternating optimization scheme ensures stability and robustness by decoupling the physics-solving and design-update steps. This inherent stability is crucial for the framework’s broad applicability, enabling it to successfully tackle both self-adjoint and challenging non-self-adjoint systems.
- **Intrinsic physics-based regularization:** The Ginzburg-Landau energy functional is incorporated into the topology network’s loss. This acts as an intrinsic regularizer, promoting well-defined designs with smooth interfaces and eliminating the need for ad-hoc density filtering schemes.
- **Direct solution of optimality conditions:** The framework fundamentally shifts the solution strategy. Instead of simulating the pseudo-time evolution of the phase-field equation, a common practice in conventional methods, APF-FNNs directly solve the system’s first-order optimality conditions for a straightforward path to the optimal design. This is accomplished by integrating the sensitivity analysis of the coupled problem with automatic differentiation, which accurately computes the total gradient of the objective functional, ensuring the phase-field is updated along the correct descent direction via backpropagation.

This paper is organized as follows. The mathematical formulation for phase-field topology optimization is established in Section 2, where the conventional L^2 gradient flow is contrasted with the proposed neural network-based alternating scheme. Section 3 then delves into the core methodology of the APF-FNNs, detailing the FNN architecture and the formulation of physics-driven loss functions for diverse multi-physics problems. The performance and versatility of the APF-FNNs are demonstrated in Section 4 across a range of 2D and 3D numerical benchmarks. The paper concludes in Section 5 with a summary of key findings and an outlook on future research directions.

2 The formulation of phase-field topology optimization

In the phase-field approach to topology optimization [55–57], the classical discrete material distribution problem is reformulated as a continuous one, governed by a phase-field variable $\phi : \Omega \subset \mathbb{R}^d$ ($d = 2, 3$), where Ω is an open bounded domain with Lipschitz continuous boundary $\partial\Omega$. This variable smoothly transitions between the material ($\phi = 1$) and the void ($\phi = 0$) phase across a diffuse interface ($0 < \phi < 1$). To resolve the inherent ill-posedness of topology optimization, this continuous framework introduces a regularization mechanism. This regularization is accomplished by augmenting the primary objective \mathcal{J}_{obj} with the Ginzburg-Landau energy $\mathcal{E}_{GL}(\phi)$. This energy term penalizes the interfacial area, which simultaneously promotes well-defined boundaries and controls the geometric complexity of the final design [56, 58].

A general phase-field topology optimization problem can be formulated as finding an optimal phase-field ϕ that solves the following constrained minimization problem.

$$\begin{aligned} \min_{\phi} \quad & \mathcal{J}(\phi) = \mathcal{J}_{\text{obj}}(\phi, \mathbf{u}) + \mathcal{E}_{GL}(\phi) + \mathcal{P}_{\text{vol}}(\phi) \\ \text{s.t.} \quad & \mathcal{R}(\phi, \mathbf{u}) = 0 \quad \text{in } \Omega, \\ & \mathcal{B}(\phi, \mathbf{u}) = 0 \quad \text{on } \partial\Omega, \end{aligned} \tag{2.1}$$

where the objective functional \mathcal{J} consists of the primary objective \mathcal{J}_{obj} , the Ginzburg-Landau energy $\mathcal{E}_{GL}(\phi)$, and a volume constraint functional $\mathcal{P}_{\text{vol}}(\phi)$. The optimization is subject to the governing state equation $\mathcal{R}(\phi, \mathbf{u}) = 0$ in the domain Ω and the boundary conditions $\mathcal{B}(\phi, \mathbf{u}) = 0$ on $\partial\Omega$. The term $\mathcal{P}_{\text{vol}}(\phi)$ enforces the volume constraint $\int_{\Omega} \phi \, d\mathbf{x} = \beta|\Omega|$ with a target volume fraction β , and can be dealt with various techniques, including the quadratic penalty [24], Lagrange multiplier or augmented Lagrangian methods [27, 57, 59].

The Ginzburg-Landau functional is defined as

$$\mathcal{E}_{GL}(\phi) = \gamma \int_{\Omega} \left(\frac{\epsilon}{2} |\nabla\phi|^2 + \frac{1}{\epsilon} W(\phi) \right) d\mathbf{x}. \tag{2.2}$$

The parameter $\gamma > 0$ scales the overall regularization effect, while $\epsilon > 0$ controls the interfacial thickness. The term $W(\phi) = \frac{1}{4}\phi^2(1-\phi)^2$ is a double-well potential. This potential promotes a binary phase distribution by establishing energy minima at the desired material ($\phi = 1$) and void ($\phi = 0$) phases [27, 55, 57, 59].

2.1 Optimization via L^2 gradient flow

A common strategy for solving the PDE-constrained optimization problem in Eq. (2.1) is to formulate it as a gradient flow. This iterative approach evolves the phase-field variable ϕ through a pseudo time $t > 0$, following the steepest descent path of the total functional $\mathcal{J}(\phi)$ [27, 58, 59]. The precise form of this evolutionary equation is determined by the choice of inner product on the function space of ϕ .

To avoid the computational expense of the fourth-order Cahn-Hilliard equation, which arises from an H^{-1} gradient flow, a popular alternative is to employ an L^2 gradient flow of the Allen-Cahn type [6, 27]. In this framework, the evolution of ϕ is governed by

$$(\partial_t \phi, \psi)_{L^2} = -\delta_{\phi} \mathcal{J}(\phi)[\psi] \quad \forall \psi \in H^1(\Omega), \tag{2.3}$$

where $(\cdot, \cdot)_{L^2}$ denotes the L^2 inner product, and $H^1(\Omega)$ is the standard Sobolev space consisting of square-integrable functions whose weak derivatives are also square-integrable. The variational derivative $\delta_{\phi} \mathcal{J}$ is the sum of three terms,

$$\delta_{\phi} \mathcal{J}(\phi)[\psi] = \delta_{\phi} \mathcal{J}_{\text{obj}}(\phi, \mathbf{u})[\psi] + \delta_{\phi} \mathcal{E}_{GL}(\phi)[\psi] + \delta_{\phi} \mathcal{P}_{\text{vol}}(\phi)[\psi]. \tag{2.4}$$

The first term $\delta_{\phi} \mathcal{J}_{\text{obj}}$ represents the sensitivity of the performance objective to a perturbation in the phase field. The second and third terms are the variational derivative of the Ginzburg-Landau energy and volume constraint, respectively. This sensitivity term is typically computed using the adjoint method, a strategy that avoids the high computational cost of directly differentiating the state variable \mathbf{u} with respect to the phase field ϕ [6].

The overall solution process follows a nested iterative scheme, as shown in Fig. 2. The outer loop, indexed by n , advances the overall optimization, while the inner loop, indexed by m , refines the phase-field design ϕ_n under a fixed set of parameters. Each outer iteration begins by solving the state and

adjoint equations to obtain the system response \mathbf{u}_n and the objective sensitivity $\delta_\phi \mathcal{J}_{\text{obj}}$, respectively. This sensitivity then drives the inner loop for M steps. Within each inner step, the design ϕ_n is evolved by solving the L^2 gradient flow in Eq. (2.3) with a semi-implicit scheme, followed by a projection to enforce the box constraint $\phi_n \in [0, 1]$. Upon completion of the inner loop, the penalty parameters for the volume constraint are updated. The entire process is repeated for N outer iterations or until convergence to a locally optimal design is achieved.

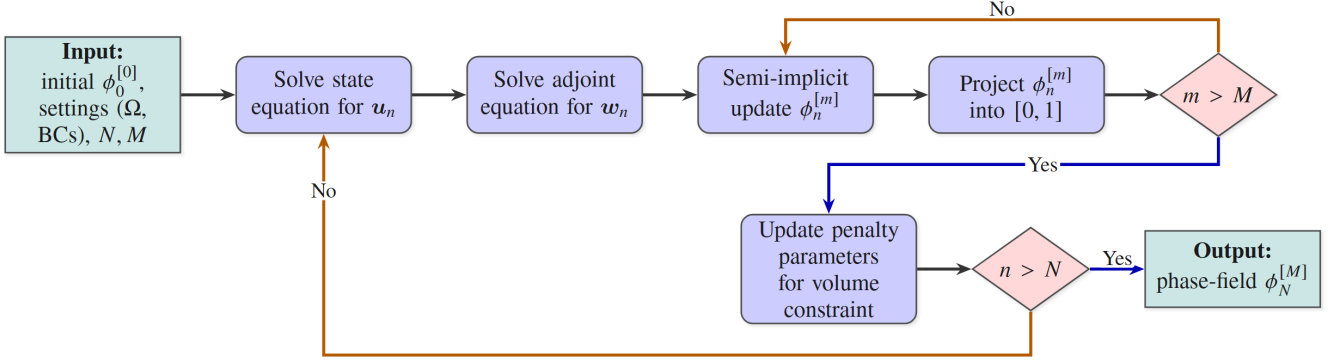


Figure 2: Flowchart of the nested iterative scheme for conventional phase-field topology optimization.

2.2 Optimization via the APF-FNNs

The proposed APF-FNNs introduce a physics-driven framework for phase-field topology optimization. Instead of iteratively solving discretized PDEs, this approach leverages the function approximation capabilities of neural networks to directly minimize the governing physical loss functions. The overall workflow, illustrated in Fig. 3, is a two-stage process that employs three distinct neural networks to parameterize the state variable $\mathbf{u}_\theta(\mathbf{x})$, the adjoint variable $\mathbf{w}_\alpha(\mathbf{x})$ and the phase-field $\phi_\sigma(\mathbf{x})$.

The optimization process commences with an **Initial Stage** to provide a robust initialization for the main alternating scheme. In this stage, the state network \mathbf{u}_θ and the adjoint network \mathbf{w}_α are sequentially pre-trained, conditioned on the initial phase-field network ϕ_σ . The networks are trained by minimizing their respective loss functions $\mathcal{L}_{\text{state}}$ and $\mathcal{L}_{\text{adjoint}}$ for a predefined number of iterations. The formulation of these losses is flexible and physics-driven: for governing equations with a known energy functional, the DRM is employed [33], whereas for systems without an explicit variational form, the PINN approach is adopted, with the loss constructed from the PDE’s strong-form residual [32].

Upon completing the initialization, the framework proceeds to the main **Alternating Optimization** stage. This stage executes a sequential training scheme where the three networks are cyclically updated. Each primary iteration n consists of three steps: (i) the state network \mathbf{u}_θ is trained for k steps by minimizing $\mathcal{L}_{\text{state}}$; (ii) using the updated state, the adjoint network \mathbf{w}_α is subsequently trained for l steps by minimizing $\mathcal{L}_{\text{adjoint}}$; and (iii) with the updated state and adjoint fields, the topology network ϕ_σ is refined for m steps. Crucially, the update of the topology network deviates from conventional methods. Instead of relying on a time-stepping L^2 gradient flow, our framework performs a direct minimization of the total objective functional \mathcal{J} from Eq. (2.1). This is achieved by defining the topology loss as the objective functional itself $\mathcal{L}_{\text{topology}}(\sigma; \mathbf{u}_\theta, \mathbf{w}_\alpha) = \mathcal{J}(\phi_\sigma, \mathbf{u}_\theta, \mathbf{w}_\alpha)$.

This formulation presents two key advantages:

- **Mesh-free formulation:** The framework is inherently mesh-free, as the neural networks operate

directly on continuous spatial coordinates \mathbf{x} . This eliminates the computational costs associated with mesh generation and refinement, a process that is particularly demanding for problems involving complex geometries and in three dimensions.

- **Efficient optimization strategy:** The unified approach is structured for computational efficiency through two complementary mechanisms:
 - **Direct gradient computation:** By integrating sensitivity analysis with automatic differentiation, the framework enables a direct gradient pathway for the topology update. This allows the gradients of the objective functional with respect to the topology network parameters σ to be computed efficiently via backpropagation, eliminating the need for an explicit and time-stepping gradient flow solver.
 - **Transfer learning and warm-starts:** The training burden is substantially reduced by a two-fold warm-start mechanism. First, pre-trained networks from the **Initial Stage** provide a high-quality initialization for the main optimization loop. Second, within the loop, parameters from the preceding iteration are used to warm-start the current one. This iterative transfer of knowledge permits the state and adjoint equations to be solved to a lower precision during intermediate steps, reducing the total computational cost per cycle.

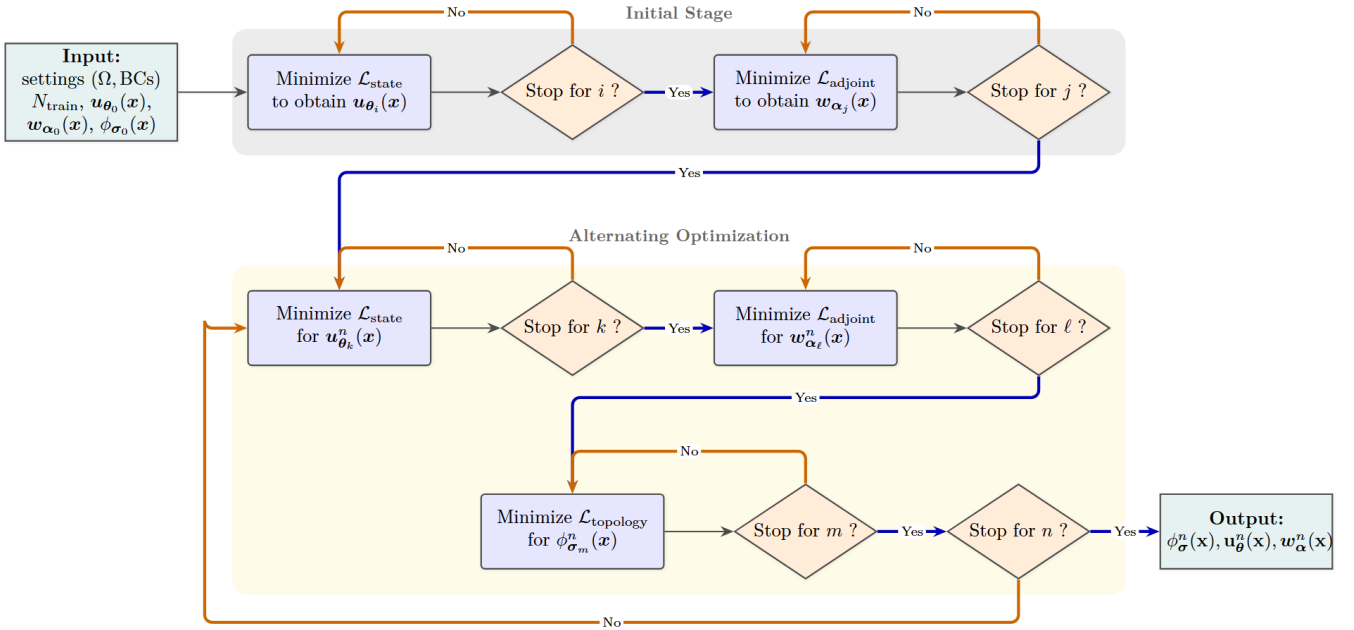


Figure 3: Flowchart of the proposed APF-FNNs. The process begins with an Initial Stage to pre-train the state and adjoint networks. This is followed by the main Alternating Optimization stage, where the neural networks for the state, adjoint and topology are refined by sequentially minimizing their respective loss functions.

3 APF-FNNs: network architectures and loss functions

As depicted in Fig. 1, the proposed APF-FNNs are built upon three distinct FNNs that parameterize the state \mathbf{u} , adjoint \mathbf{w} and phase-field ϕ variables. These networks are trained jointly using an alternating

optimization scheme, where the process is guided by specific loss functions derived from the governing physics. The following subsections will detail the FNN architecture and the formulation of loss functions.

3.1 Fourier neural network architecture

Multi-Layer Perceptrons (MLPs) suffer from spectral bias, an inability to effectively learn high-frequency functions, which limits their performance on tasks involving sharp interfaces or complex geometries [34, 60]. The Fourier Neural Network (FNN) architecture, illustrated in the first row of Fig. 1, mitigates this by first transforming the low-dimensional input coordinates \mathbf{x} into a high-dimensional feature space using the following mapping

$$\Gamma(\mathbf{x}) = [\cos(2\pi\mathbf{B}\mathbf{x}), \sin(2\pi\mathbf{B}\mathbf{x})]^T. \quad (3.1)$$

This frequency matrix \mathbf{B} is populated at initialization by sampling from a Gaussian distribution with a mean of zero and a standard deviation. The hyperparameter deviation governs the frequency range of the sinusoidal mapping. This initial encoding enables the subsequent MLP to capture fine details, overcoming the spectral bias inherent to standard architectures.

The resulting feature vector $\Gamma(\mathbf{x}) \in \mathbb{R}^{2m}$ is subsequently processed by a MLP to produce the final output $f(\mathbf{x}; \boldsymbol{\xi}) \in \mathbb{R}^{d_{\text{out}}}$. The MLP consists of L hidden layers, each with n_l neurons for $l = 1, \dots, L$. The input to the MLP is the Fourier feature vector defined as $\mathbf{h}^{(0)} = \Gamma(\mathbf{x})$. The computation proceeds recursively through the hidden layers

$$\mathbf{h}^{(l)} = \mathcal{S}(\mathbf{W}^{(l)}\mathbf{h}^{(l-1)} + \mathbf{b}^{(l)}), \quad \text{for } l = 1, 2, \dots, L, \quad (3.2)$$

where for the l -th layer, $\mathbf{W}^{(l)} \in \mathbb{R}^{n_l \times n_{l-1}}$ and $\mathbf{b}^{(l)} \in \mathbb{R}^{n_l}$ represent the weight matrix and bias vector, respectively, while \mathcal{S} is a non-linear activation function. Finally, a linear output layer computes the network's final prediction

$$f(\mathbf{x}; \boldsymbol{\xi}) = \mathbf{W}^{(L+1)}\mathbf{h}^{(L)} + \mathbf{b}^{(L+1)}, \quad (3.3)$$

where $\mathbf{W}^{(L+1)} \in \mathbb{R}^{d_{\text{out}} \times n_L}$ and $\mathbf{b}^{(L+1)} \in \mathbb{R}^{d_{\text{out}}}$ are the output layer parameters. Consequently, the complete set of trainable parameters for the FNN comprises two distinct components: the Fourier mapping matrix \mathbf{B} and the set of MLP parameters $\boldsymbol{\xi} = \{\mathbf{W}^{(l)}, \mathbf{b}^{(l)}\}_{l=1}^{L+1}$.

The capacity to efficiently represent high-frequency components makes the FNN exceptionally well-suited for problems requiring fine-grained detail. This makes the architecture a powerful tool for modeling both smooth physical fields and complex geometric designs, proving highly effective in applications like topology optimization [52, 60]. Architecturally, all three modules in APF-FNNs are implemented as FNNs with sine activation functions in all hidden layers. The crucial exception is the output layer of the topology FNN, which is equipped with a sigmoid function. This final activation enforces the box constraint $\phi(\mathbf{x}) \in [0, 1]$ automatically, which is essential for the phase-field formulation and avoids the need for post-processing steps like projection or clamping.

3.2 Loss function formulation

The APF-FNNs rely on training FNNs by minimizing specific loss functions. These loss functions are formulated from either the variational principles or the strong form of the governing PDEs for a specific problem. The training process sequentially minimizes these losses, following the proposed alternating optimization scheme in Fig. 3. To demonstrate the efficacy of this approach, four distinct topology optimization problems are addressed, covering both self-adjoint and non-self-adjoint cases. The self-adjoint problems include compliance minimization and first eigenvalue maximization in linear elasticity, as well as Stokes flow. For the non-self-adjoint case, the optimization governed by Navier-Stokes flow is considered. The

self-adjoint nature of the first three problems permits a significant framework simplification: the state and adjoint variables become equivalent, which obviates the need for a dedicated adjoint network and streamlines the optimization workflow.

3.2.1 Compliance minimization in linear elasticity

The governing equation for linear elasticity is self-adjoint, originating from the principle of minimum potential energy. This allows the use of a variational approach to solve for the displacement field \mathbf{u}_θ by minimizing a single energy functional. Accordingly, the loss function for the state network $\mathcal{L}_{\text{state}}$ is defined as the total potential energy of the system, augmented with a penalty term to enforce Dirichlet boundary conditions.

The material distribution is described by the interpolated elasticity tensor $\mathbb{C}(\phi_\sigma)$ which is defined through a SIMP penalization scheme

$$\mathbb{C}(\phi_\sigma) = \rho(\phi_\sigma)\mathbb{C}_0, \quad \text{with} \quad \rho(\phi_\sigma) = (1 - \phi_{\min})\phi_\sigma^p + \phi_{\min}.$$

Here the integer $p > 1$ is the penalization factor, and ϕ_{\min} is a small positive constant to prevent singularity. The base material is assumed to be isotropic, with \mathbb{C}_0 being the symmetric fourth-order elasticity tensor

$$\mathbb{C}_0 \boldsymbol{\varepsilon} = 2\mu \boldsymbol{\varepsilon} + \lambda \text{tr}(\boldsymbol{\varepsilon})I,$$

where $\text{tr}(\cdot)$ is the trace operator, I is the identity matrix, and the Lamé parameters μ and λ are defined by the Young's modulus E and Poisson's ratio ν as

$$\mu = \frac{E}{2(1 + \nu)} \quad \text{and} \quad \lambda = \frac{E\nu}{(1 + \nu)(1 - 2\nu)},$$

respectively.

With these definitions, the complete loss function for the state network is given by

$$\mathcal{L}_{\text{state}}(\boldsymbol{\theta}; \phi_\sigma) = \frac{1}{2} \int_{\Omega} \mathbb{C}(\phi_\sigma) \boldsymbol{\varepsilon}(\mathbf{u}_\theta) : \boldsymbol{\varepsilon}(\mathbf{u}_\theta) \, d\mathbf{x} - \int_{\Omega} \mathbf{b} \cdot \mathbf{u}_\theta \, d\mathbf{x} - \int_{\Gamma_N} \mathbf{t} \cdot \mathbf{u}_\theta \, ds + \lambda_{\text{Dir}} \int_{\Gamma_D} (\mathbf{u}_\theta - \mathbf{u}_0)^2 \, ds, \quad (3.4)$$

where $\boldsymbol{\varepsilon}(\mathbf{u}_\theta) = \frac{1}{2}(\nabla \mathbf{u}_\theta + \nabla \mathbf{u}_\theta^T)$ is the symmetric strain tensor. The terms \mathbf{b} and \mathbf{t} represent the body and surface forces, respectively. The final term enforces the prescribed displacement \mathbf{u}_0 on the Dirichlet boundary Γ_D with λ_{Dir} serving as the penalty parameter.

The topology network ϕ_σ is updated by minimizing an objective functional that corresponds to the structural compliance. The topology loss $\mathcal{L}_{\text{design}}$ incorporates this compliance objective along with two crucial regularization terms formulated as follows

$$\mathcal{L}_{\text{topology}}(\boldsymbol{\sigma}; \mathbf{u}_\theta) = \left(\int_{\Omega} \mathbf{b} \cdot \mathbf{u}_\theta \, d\mathbf{x} + \int_{\Gamma_N} \mathbf{t} \cdot \mathbf{u}_\theta \, ds \right) + \mathcal{E}_{GL}(\phi_\sigma) + \mathcal{P}_{\text{vol}}(\phi_\sigma). \quad (3.5)$$

The volume penalty term which enforces a target volume fraction $\beta \in (0, 1)$ is given by

$$\mathcal{P}_{\text{vol}}(\phi_\sigma) = \lambda_{\text{penal}} \left(\int_{\Omega} \phi_\sigma \, d\mathbf{x} - \beta |\Omega| \right)^2,$$

where $\lambda_{\text{penal}} > 0$ is a penalty parameter. This formulation enables the direct minimization of compliance, while the regularization terms ensure a well-posed optimization problem with a specified material volume.

3.2.2 First eigenvalue maximization in linear elasticity

The objective in this problem is to maximize the fundamental natural frequency of a structure, a crucial design goal for preventing resonance with external dynamic loads. This is mathematically equivalent to maximizing the first eigenvalue λ_1 of the system. The optimization framework is based on the variational principle of the Rayleigh quotient. Physically, the Rayleigh quotient represents the ratio of the maximum strain energy to the maximum kinetic energy. This principle states that the first eigenvalue is the minimum value of this quotient over all kinematically admissible displacement fields. Therefore, the problem is formulated as a min-max optimization, where the goal is to find a design that maximizes the minimal value of the Rayleigh quotient.

For a fixed material distribution ϕ_σ , the state network is trained to approximate the fundamental mode \mathbf{u}_θ . According to the variational principle, this is achieved by finding the function that minimizes the Rayleigh quotient. To ensure the uniqueness of the eigenfunction, which is otherwise only defined up to a scalar multiple, a mass normalization constraint is imposed by $\int_\Omega \varrho(\phi) \|\mathbf{u}\|^2 d\mathbf{x} = 1$. The loss function for the state network $\mathcal{L}_{\text{state}}$ combines the Rayleigh quotient objective with a quadratic penalty to enforce this normalization constraint

$$\mathcal{L}_{\text{state}}(\boldsymbol{\theta}; \phi_\sigma) = \frac{\int_\Omega \mathbb{C}(\phi_\sigma) \boldsymbol{\varepsilon}(\mathbf{u}_\theta) : \boldsymbol{\varepsilon}(\mathbf{u}_\theta) d\mathbf{x}}{\int_\Omega \varrho(\phi_\sigma) \mathbf{u}_\theta^2 d\mathbf{x}} + \lambda_{\text{norm}} \left(\int_\Omega \varrho(\phi_\sigma) \mathbf{u}_\theta^2 d\mathbf{x} - 1 \right)^2, \quad (3.6)$$

where $\varrho(\phi_\sigma) = (1 - \phi_{\min})\phi_\sigma + \phi_{\min}$ is the interpolated material density, and λ_{norm} is the penalty parameter.

The APF-FNNs are trained using an alternating optimization scheme that iterates between the two coupled networks. In the first step, the state network parameters are optimized by minimizing $\mathcal{L}_{\text{state}}$ for a fixed topology ϕ_σ , yielding the fundamental eigenmode \mathbf{u}_θ . In the second step, the topology network is updated to maximize the resulting eigenvalue. This is achieved by minimizing the topology loss function, $\mathcal{L}_{\text{topology}}$, which is defined as:

$$\mathcal{L}_{\text{topology}}(\boldsymbol{\sigma}; \mathbf{u}_\theta) = -\frac{\int_\Omega \mathbb{C}(\phi_\sigma) \boldsymbol{\varepsilon}(\mathbf{u}_\theta) : \boldsymbol{\varepsilon}(\mathbf{u}_\theta) d\mathbf{x}}{\int_\Omega \varrho(\phi_\sigma) \mathbf{u}_\theta^2 d\mathbf{x}} + \mathcal{E}_{GL}(\phi_\sigma) + \mathcal{P}_{\text{vol}}(\phi_\sigma). \quad (3.7)$$

This loss function combines the negative Rayleigh quotient with regularization terms for geometric complexity \mathcal{E}_{GL} and volume constraint \mathcal{P}_{vol} .

3.2.3 Stokes flow optimization

Topology optimization for Stokes flow seeks to minimize power dissipation, defined as the sum of viscous dissipation and the work done by body forces [61]. The optimization is constrained by the Stokes equations, a saddle-point problem for velocity \mathbf{u} and pressure p . PINNs are leveraged as a natural framework to solve this coupled and constrained system.

For a fixed phase-field ϕ_σ , a single state network with parameters $\boldsymbol{\theta}$ is trained to approximate both the velocity field \mathbf{u}_θ and the pressure field p_θ . The network is trained by minimizing a physics-informed loss function $\mathcal{L}_{\text{state}}$ composed of four squared-residual terms. These terms enforce the momentum balance, the incompressibility constraint, the Dirichlet and Neumann boundary conditions. The complete loss function is formulated as follows.

$$\begin{aligned} \mathcal{L}_{\text{state}}(\boldsymbol{\theta}; \phi_\sigma) = & \int_\Omega (-\mu \Delta \mathbf{u}_\theta + \nabla p_\theta + \Pi(\phi_\sigma) \mathbf{u}_\theta - \mathbf{f})^2 d\mathbf{x} \\ & + \lambda_{\text{div}} \int_\Omega (\nabla \cdot \mathbf{u}_\theta)^2 d\mathbf{x} + \lambda_{\text{Dir}} \int_{\Gamma_D} (\mathbf{u}_\theta - \mathbf{g})^2 ds \\ & + \lambda_{\text{Neu}} \int_{\Gamma_N} ((-p_\theta \mathbf{I} + \mu(\nabla \mathbf{u}_\theta + \nabla \mathbf{u}_\theta^T)) \mathbf{n} - \mathbf{h})^2 ds. \end{aligned} \quad (3.8)$$

Here, μ is the fluid viscosity and \mathbf{f} is a body force. The friction term $\Pi(\phi_\sigma) = \eta(1 - \phi_\sigma)^2$ with penalty $\eta > 0$ models the presence of the material phase. Prescribed velocities \mathbf{g} and tractions \mathbf{h} are enforced on the Dirichlet and Neumann boundaries, respectively. The terms λ_{div} , λ_{Dir} and λ_{Neu} are hyper-parameters that weight the contribution of each loss component.

The topology network is trained to minimize the total power dissipated by the fluid. This objective is represented by the topology loss $\mathcal{L}_{\text{design}}$ which is formulated as

$$\mathcal{L}_{\text{topology}}(\boldsymbol{\sigma}; \mathbf{u}_\theta) = \int_{\Omega} \left(\frac{1}{2} \Pi(\phi_\sigma) |\mathbf{u}_\theta|^2 + \frac{\mu}{2} |\nabla \mathbf{u}_\theta|^2 - \mathbf{f} \cdot \mathbf{u}_\theta \right) d\mathbf{x} + \mathcal{E}_{GL}(\phi_\sigma) + \mathcal{P}_{\text{vol}}(\phi_\sigma). \quad (3.9)$$

The volume constraint is handled as previously described. During the topology update step of the alternating scheme, this loss is minimized with respect to the design parameters $\boldsymbol{\sigma}$. This approach, which leverages a pre-computed state field \mathbf{u}_θ , decouples the gradient calculation from the state network's parameters, significantly stabilizing and accelerating the optimization process.

3.2.4 Navier-Stokes flow optimization

When inertial effects become significant, particularly at moderate to high Reynolds numbers, the linear Stokes model is no longer a valid approximation of the fluid dynamics. The problem is therefore extended to the incompressible Navier-Stokes equations. This requires the inclusion of the nonlinear convective term $(\mathbf{u} \cdot \nabla) \mathbf{u}$ in the momentum balance, which accounts for the transport of momentum by the flow itself.

To accommodate the Navier-Stokes physics, the state loss function $\mathcal{L}_{\text{state}}$ is adapted from the Stokes formulation by incorporating the nonlinear convective term into the momentum equation's residual. The modified loss is

$$\begin{aligned} \mathcal{L}_{\text{state}}(\boldsymbol{\theta}; \phi_\sigma) &= \int_{\Omega} ((\mathbf{u}_\theta \cdot \nabla) \mathbf{u}_\theta - \mu \Delta \mathbf{u}_\theta + \nabla p_\theta + \Pi(\phi_\sigma) \mathbf{u}_\theta - \mathbf{f})^2 d\mathbf{x} \\ &+ \lambda_{\text{div}} \int_{\Omega} (\nabla \cdot \mathbf{u}_\theta)^2 d\mathbf{x} + \lambda_{\text{Dir}} \int_{\Gamma_D} (\mathbf{u}_\theta - \mathbf{g})^2 ds \\ &+ \lambda_{\text{Neu}} \int_{\Gamma_N} ((-p_\theta \mathbf{I} + \mu(\nabla \mathbf{u}_\theta + \nabla \mathbf{u}_\theta^T)) \mathbf{n} - \mathbf{h})^2 ds. \end{aligned} \quad (3.10)$$

The terms enforcing the incompressibility constraint and the boundary conditions remain identical to those in the Stokes formulation. The inclusion of this single nonlinear term, however, fundamentally changes the character of the state problem, making its solution considerably more challenging.

While the topology loss function $\mathcal{L}_{\text{topology}}$ is formally identical to the Stokes case and still represents the regularized power dissipation, a critical distinction arises from the state field used in its evaluation.

$$\mathcal{L}_{\text{topology}}(\boldsymbol{\sigma}; \mathbf{u}_\theta, \mathbf{w}_\alpha) = \int_{\Omega} \left(\frac{1}{2} \Pi(\phi_\sigma) |\mathbf{u}_\theta|^2 + \frac{\mu}{2} |\nabla \mathbf{u}_\theta|^2 - \mathbf{f} \cdot \mathbf{u}_\theta \right) d\mathbf{x} + \mathcal{E}_{GL}(\phi_\sigma) + \mathcal{P}_{\text{vol}}(\phi_\sigma). \quad (3.11)$$

Specifically, the velocity field \mathbf{u}_θ is now the solution to the nonlinear Navier-Stokes equations. This non-linearity breaks the self-adjoint property of the system, necessitating the introduction of an adjoint field \mathbf{w}_α for an efficient and accurate sensitivity analysis.

The required sensitivities are computed by solving for an adjoint field \mathbf{w}_α which is governed by the following continuous adjoint equations.

$$\begin{aligned} (\nabla \mathbf{u}_\theta)^T \mathbf{w} - (\mathbf{u}_\theta \cdot \nabla) \mathbf{w} - \mu \Delta \mathbf{w} + \nabla q + \Pi(\phi_\sigma) \mathbf{w} + \frac{\delta \mathcal{J}}{\delta \mathbf{u}_\theta} &= 0 \quad \text{in } \Omega, \\ \nabla \cdot \mathbf{w} &= 0 \quad \text{in } \Omega, \end{aligned} \quad (3.12)$$

where \mathbf{w} and q are the adjoint velocity and pressure fields, respectively. The final term in the momentum equation $\frac{\delta \mathcal{J}}{\delta \mathbf{u}_\theta}$ is the functional derivative of the objective \mathcal{J} with respect to the state velocity. For the power dissipation objective, this derivative is explicitly $\Pi(\phi_\sigma)\mathbf{u}_\theta - \mu\Delta\mathbf{u}_\theta - \mathbf{f}$. The system is typically closed by applying homogeneous boundary conditions to the adjoint variables.

A second adjoint network with parameters α is introduced to approximate the adjoint fields $(\mathbf{w}_\alpha, q_\alpha)$. This network is trained by minimizing an adjoint loss, $\mathcal{L}_{\text{adjoint}}$, which penalizes the residuals of the adjoint equations (3.12) and their boundary conditions.

$$\begin{aligned} \mathcal{L}_{\text{adjoint}}(\alpha; \mathbf{u}_\theta, \phi_\sigma) = & \int_{\Omega} \left((\nabla\mathbf{u}_\theta)^T \mathbf{w}_\alpha - (\mathbf{u}_\theta \cdot \nabla) \mathbf{w}_\alpha - \mu\Delta\mathbf{w}_\alpha \right. \\ & \left. + \nabla q_\alpha + \Pi(\phi_\sigma)\mathbf{w}_\alpha - \mu\Delta\mathbf{u}_\theta + \Pi(\phi_\sigma)\mathbf{u}_\theta - \mathbf{f} \right)^2 d\mathbf{x} \\ & + \lambda_{\text{adj,div}} \int_{\Omega} (\nabla \cdot \mathbf{w}_\alpha)^2 d\mathbf{x} + \lambda_{\text{adj,BC}} \int_{\Gamma_D} \mathbf{w}_\alpha^2 ds \\ & + \lambda_{\text{adj,Neu}} \int_{\Gamma_N} \left(\left(-q_\alpha \mathbf{I} + \mu(\nabla\mathbf{w}_\alpha + \nabla\mathbf{w}_\alpha^T) \right) \mathbf{n} \right)^2 ds. \end{aligned} \quad (3.13)$$

Consequently, the alternating optimization scheme is extended to a three-step iterative process. Within each iteration, the framework first solves for the state fields $(\mathbf{u}_\theta, p_\theta)$ by minimizing $\mathcal{L}_{\text{state}}$. Next, it solves for the corresponding adjoint fields \mathbf{w}_α using the computed state. Finally, the topology parameters σ are updated by minimizing $\mathcal{L}_{\text{topology}}$, where the gradient calculation leverages both the state and adjoint fields.

4 Numerical Experiments

A crucial aspect of leveraging APF-FNNs for topology optimization is the accurate evaluation of the total gradient for the objective functional $\mathcal{L}_{\text{topology}}$. A naive application of automatic differentiation (AD) to the topology network's loss function is inherently flawed. This is because standard AD only differentiates through the explicit computational graph, thereby capturing the direct sensitivity of the objective to the design parameters σ . However, it critically overlooks the implicit sensitivity that stems from the physical coupling: the state variable \mathbf{u}_θ is governed by a PDE that is parameterized by the phase-field ϕ_σ , making \mathbf{u}_θ an implicit function of the design. By disregarding this coupling, standard AD computes only the explicit portion of the total gradient by

$$\nabla_{\sigma}^{\text{AD}} \mathcal{L}_{\text{topology}} = \frac{\partial \mathcal{J}_{\text{obj}}(\phi_\sigma, \mathbf{u}_\theta)}{\partial \sigma} + \frac{d\mathcal{E}_{GL}(\phi_\sigma)}{d\sigma} + \frac{d\mathcal{P}_{\text{vol}}(\phi_\sigma)}{d\sigma}. \quad (4.1)$$

However, a physically rigorous optimization must be guided by the total derivative. Applying the chain rule, this total derivative of the coupled loss function decomposes into the following two distinct components.

$$\begin{aligned} \frac{d\mathcal{L}_{\text{topology}}}{d\sigma} &= \frac{d\mathcal{J}_{\text{obj}}(\phi_\sigma, \mathbf{u}_\theta)}{d\sigma} + \frac{d\mathcal{E}_{GL}(\phi_\sigma)}{d\sigma} + \frac{d\mathcal{P}_{\text{vol}}(\phi_\sigma)}{d\sigma} \\ &= \underbrace{\frac{\partial \mathcal{J}_{\text{obj}}}{\partial \sigma} + \frac{d\mathcal{E}_{GL}(\phi_\sigma)}{d\sigma} + \frac{d\mathcal{P}_{\text{vol}}(\phi_\sigma)}{d\sigma}}_{\text{Explicit term}} + \underbrace{\frac{\partial \mathcal{J}_{\text{obj}}}{\partial \mathbf{u}_\theta} \frac{d\mathbf{u}_\theta}{d\sigma}}_{\text{Implicit term}} \\ &= \nabla_{\sigma}^{\text{AD}} \mathcal{L}_{\text{topology}} + \frac{\partial \mathcal{J}_{\text{obj}}}{\partial \mathbf{u}_\theta} \frac{d\mathbf{u}_\theta}{d\sigma}. \end{aligned} \quad (4.2)$$

A standard AD framework, which does not differentiate through the PDE solver, evaluates only the explicit term. It is therefore blind to the implicit term, which is crucial for accurate gradient-based optimization.

This term, arising from the intractable derivative of the state with respect to the design $\frac{d\mathbf{u}_\theta}{d\boldsymbol{\sigma}}$, is non-zero and cannot be neglected. To bridge this critical discrepancy and ensure the optimization is driven by physically-grounded gradients, the results from AD must be benchmarked against a trusted sensitivity analysis method. This verification is fundamental to achieving a meaningful and converged optimal design.

To validate the proposed APF-FNNs, we present a series of numerical experiments spanning the four distinct physics problems described in Section 3.2. The optimization follows a unified alternating scheme, detailed in Algorithm 1, whose structure adapts based on the problem’s physical properties.

For non-self-adjoint systems, such as Navier-Stokes flow, the complete optimization process is employed, utilizing three distinct FNNs for the state, adjoint, and topology fields. Conversely, for self-adjoint problems (compliance minimization, eigenvalue maximization, and Stokes flow), the framework simplifies significantly. In these cases, the state and adjoint variables are equivalent, making a dedicated adjoint network and its associated optimization step unnecessary. The process thus becomes a more direct alternating optimization between only the state and topology networks.

Across all experiments, FNNs parameterizing the physical fields employ sine activation functions in their hidden layers. The topology network, which outputs the phase-field variable ϕ , is uniquely equipped with a final sigmoid activation to naturally enforce the box constraint $\phi \in [0, 1]$. Integrals in the loss functions are approximated using Monte Carlo integration over a set of N_{train} collocation points randomly sampled from the domain Ω and its boundaries $\partial\Omega$. All networks are trained using the Adam optimizer. The framework is implemented in Python using TensorFlow, with experiments conducted on a single NVIDIA RT 4090 GPU.

4.1 Compliance minimization in linear elasticity

A critical step is to validate the gradients computed by AD for the topology network against the established adjoint method for sensitivity analysis. For compliance minimization, the adjoint method provides the true sensitivity of the objective \mathcal{J}_{obj} with respect to the phase-field variable ϕ_σ , which is proportional to the negative strain energy density, as formally expressed by

$$\frac{d\mathcal{J}_{\text{obj}}}{d\phi_\sigma} = - \int_{\Omega} \frac{\partial \mathcal{C}(\phi_\sigma)}{\partial \phi_\sigma} \boldsymbol{\varepsilon}(\mathbf{u}_\theta) : \boldsymbol{\varepsilon}(\mathbf{u}_\theta) dx. \quad (4.3)$$

In contrast, a standard AD framework evaluating the compliance term in $\mathcal{L}_{\text{topology}}$ computes a gradient equal to the positive strain energy density

$$\frac{\partial \mathcal{J}_{\text{obj}}}{\partial \phi_\sigma} = \int_{\Omega} \frac{\partial \mathcal{C}(\phi_\sigma)}{\partial \phi_\sigma} \boldsymbol{\varepsilon}(\mathbf{u}_\theta) : \boldsymbol{\varepsilon}(\mathbf{u}_\theta) dx. \quad (4.4)$$

This leads to the fundamental relationship

$$\frac{d\mathcal{J}_{\text{obj}}}{d\phi_\sigma} = - \frac{\partial \mathcal{J}_{\text{obj}}}{\partial \phi_\sigma}. \quad (4.5)$$

This identity reveals that a naively applied AD gradient would perform maximization, moving the design in the exact opposite direction of compliance minimization. To resolve this, we employ a robust hybrid approach. Instead of differentiating the entire computational graph, AD is leveraged solely for its efficiency in evaluating the strain energy density. A custom and physically-derived gradient is then constructed for the backpropagation step by negating this value. This technique circumvents the known instabilities of purely AD-based differentiation and ensures the optimization is guided by the stable and physically rigorous principles of the traditional adjoint method.

Algorithm 1: APF-FNNs: Alternating Phase-Field Fourier Neural Networks

Input:

β : Target volume fraction;
 \mathbf{X} : Training coordinates within the design domain Ω ;
 \mathbf{X}_b : Non-homogenous Neumann boundary coordinates;
 $\text{LR}_{\theta, \text{init}}, \text{LR}_{\theta, \text{opt}}, \text{LR}_{\alpha}, \text{LR}_{\sigma}$: Learning rates;
 $\lambda_{\text{penal}}^{(0)}, \zeta$: Initial penalty parameter and its scaling factor;
 ϵ, γ : Regularization parameters for the phase-field model;
 I, N : Epochs for initial fitting and total optimization;
 K, L, M : Inner-loop iterations for state, adjoint and design updates;

1 Initialize:

2 State network $\mathbf{u}_{\theta}(\mathbf{x})$ with parameters $\theta^{(0)}$;
 3 Topology network $\phi_{\sigma}(\mathbf{x})$ with parameters $\sigma^{(0)}$;
 4 Adam optimizers for three networks;

6 Fix $\sigma^{(0)}$ and obtain the initial design $\phi_{\sigma^{(0)}}(\mathbf{x})$;

7 // Stage 1: Initial field estimations

8 for $i = 1$ to I do

9 Compute loss $\mathcal{L}_{\text{state}}(\theta^{(i-1)}; \phi_{\sigma^{(0)}})$;
 10 Update state network: $\theta^{(i)} \leftarrow \text{Adam}(\theta^{(i-1)}, \nabla_{\theta} \mathcal{L}_{\text{state}})$;

12 $\theta_0^{(0)} \leftarrow \theta^{(I)}$, $\alpha_0^{(0)} \leftarrow \theta^{(I)}$ and $\sigma_0^{(0)} \leftarrow \sigma^{(0)}$;

13 // Stage 2: Alternating optimization

14 for $n = 1$ to N do

15 Update penalty: $\lambda_{\text{penal}}^{(n)} \leftarrow \lambda_{\text{penal}}^{(n-1)} / \zeta$;

16 // Optimize state \mathbf{u}_{θ}

17 Fix design parameters $\sigma_{n-1}^{(0)}$;

18 for $k = 1$ to K do

19 Compute loss $\mathcal{L}_{\text{state}}(\theta_{n-1}^{(k-1)}; \phi_{\sigma_{n-1}^{(0)}})$;

20 Update state network parameters: $\theta_{n-1}^{(k)} \leftarrow \text{Adam}(\theta_{n-1}^{(k-1)}, \nabla_{\theta} \mathcal{L}_{\text{state}})$;

21 $\theta_n^{(0)} \leftarrow \theta_{n-1}^{(K)}$;

22 // Optimize adjoint \mathbf{w}_{α}

23 Fix design parameters $\sigma_{n-1}^{(0)}, \theta_n^{(0)}$;

24 for $k = 1$ to K do

25 Compute loss $\mathcal{L}_{\text{adjoint}}(\alpha_{n-1}^{(k-1)}; \phi_{\sigma_{n-1}^{(0)}}, \theta_n^{(0)})$;

26 Update adjoint network parameters: $\alpha_{n-1}^{(k)} \leftarrow \text{Adam}(\alpha_{n-1}^{(k-1)}, \nabla_{\alpha} \mathcal{L}_{\text{adjoint}})$;

27 // Optimize phase field ϕ_{σ}

28 for $m = 1$ to M do

29 Compute loss $\mathcal{L}_{\text{topology}}(\sigma_{n-1}^{(m-1)}; \mathbf{u}_{\theta_n^{(0)}}, \mathbf{w}_{\alpha_n^{(0)}})$;

30 Update design network via adjoint method: $\sigma_{n-1}^{(m)} \leftarrow \text{Adam}(\sigma_{n-1}^{(m-1)}, \nabla_{\sigma} \mathcal{L}_{\text{topology}})$;

31 $\sigma_n^{(0)} \leftarrow \sigma_{n-1}^{(M)}$;

Output: The optimized parameters $\theta_N^{(0)}$, $\alpha_N^{(0)}$ and $\sigma_N^{(0)}$.

4.1.1 Compliance minimization in two dimensions

The proposed method is validated on three classic 2D minimum compliance benchmarks, as illustrated in Fig. 4. All examples share a rectangular design domain $\Omega = (-1, 1) \times (-0.5, 0.5)$ and common physical parameters: an isotropic linear elastic material with $E = 1.0$ and $\nu = 0.3$, a SIMP penalization factor of $p = 3$, and zero body force $\mathbf{b} = \mathbf{0}$. Any boundary not explicitly constrained is assumed to be traction-free. The three benchmark cases are defined by their distinct boundary conditions:

- (a) **Cantilever beam:** A standard cantilever setup where the left boundary is clamped on $\Gamma_D = \{0\} \times (-0.5, 0.5)$, and a downward point load $\mathbf{t} = (0, -1)^T$ is applied to the center of the right boundary on $\Gamma_N = \{1\} \times (-0.05, 0.05)$.
- (b) **Offset-loaded beam:** This case modifies the cantilever setup by relocating the load to the bottom-right corner, on the segment $\Gamma_N = \{1\} \times (-0.5, -0.4)$, while keeping the left boundary clamped.
- (c) **MBB beam:** A classic Messerschmitt-Bölkow-Blohm (MBB) beam, supported at the two bottom corners on $\Gamma_D = (-1, -0.95) \times \{-0.5\} \cup (0.95, 1) \times \{-0.5\}$ and subjected to a downward load at the center of its bottom edge with $\Gamma_N = (-0.05, 0.05) \times \{-0.5\}$.

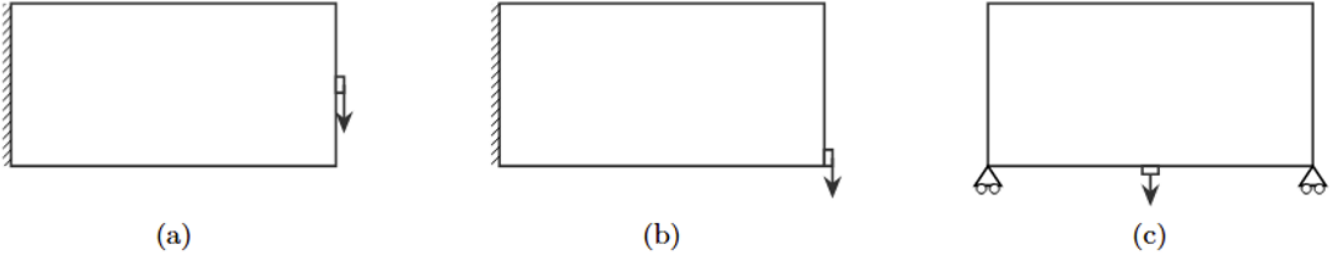


Figure 4: Problem setups for the three 2D compliance minimization benchmarks: (a) Cantilever beam, (b) Offset-loaded beam, and (c) MBB beam.

The key hyperparameters and network settings are held consistent across the three benchmarks. The physical and numerical parameters are detailed below.

- A target volume fraction of $\beta = 0.5$ is used, with a minimum phase-field value of $\phi_{\min} = 10^{-4}$. The phase-field regularization parameters were set to $\epsilon = \gamma = 10^{-2}$.
- The domain Ω is discretized with a set of 20,000 collocation points for the interior and 500 points for the non-homogeneous Neumann boundary Γ_N .
- The volume constraint is enforced using a penalty method. The penalty parameter is initialized to $\lambda_{\text{penal}}^{(0)} = 1$ and dynamically scaled by a factor of $\zeta = 0.98$ each epoch.

A key distinction between the cases lies in the enforcement of homogeneous Dirichlet boundary conditions. For the cantilever setups (cases (a) and (b)), the zero-displacement condition on the left boundary is enforced by construction. This is achieved by multiplying the state network’s output by a distance function $(\mathbf{x}_2 + 1)$, which is zero on the boundary and non-zero elsewhere. For the MBB beam (case (c)), the clamped conditions at the bottom corners were enforced as a soft constraint via a penalty term in the loss function, using 500 collocation points on Γ_D with a penalty weight of $\lambda_{\text{Dir}} = 5$.

The state and design fields are parameterized by two distinct FNNs. The state network, which maps a 2D coordinate to a 2D displacement vector, consists of a single hidden layer with 2304 sine-activated neurons. The design network, mapping a 2D coordinate to the scalar phase-field, uses one hidden layer of 576 sine-activated neurons, followed by a final sigmoid activation to constrain its output to the range $[0, 1]$. Both networks are initialized deterministically following the procedure in [52], where the first layer’s frequency components are set on a uniform grid (up to 35 for the state and 30 for the topology network). These frequency kernels are trainable, and the final layer weights are initialized to zero to ensure a stable optimization starting point.

The training procedure involves a two-stage learning rate for the state network and a scheduled number of updates for the topology network. The state network is first pre-trained with a learning rate of 10^{-3} until the relative variational error of the linear elasticity equation falls below 10^{-3} (minimum 1000 iterations). During the main alternating optimization, its learning rate is reduced to 10^{-4} . The topology network uses a constant learning rate of 10^{-3} . The total optimization runs for $N = 500$ epochs. In each epoch, the state network is updated $K = 20$ times. The number of design updates, M , is scheduled: M is set to 1 for the first 200 epochs, and subsequently increased to $M = 10$ for cases (a) and (c), and $M = 20$ for case (b) for the remaining 300 epochs.

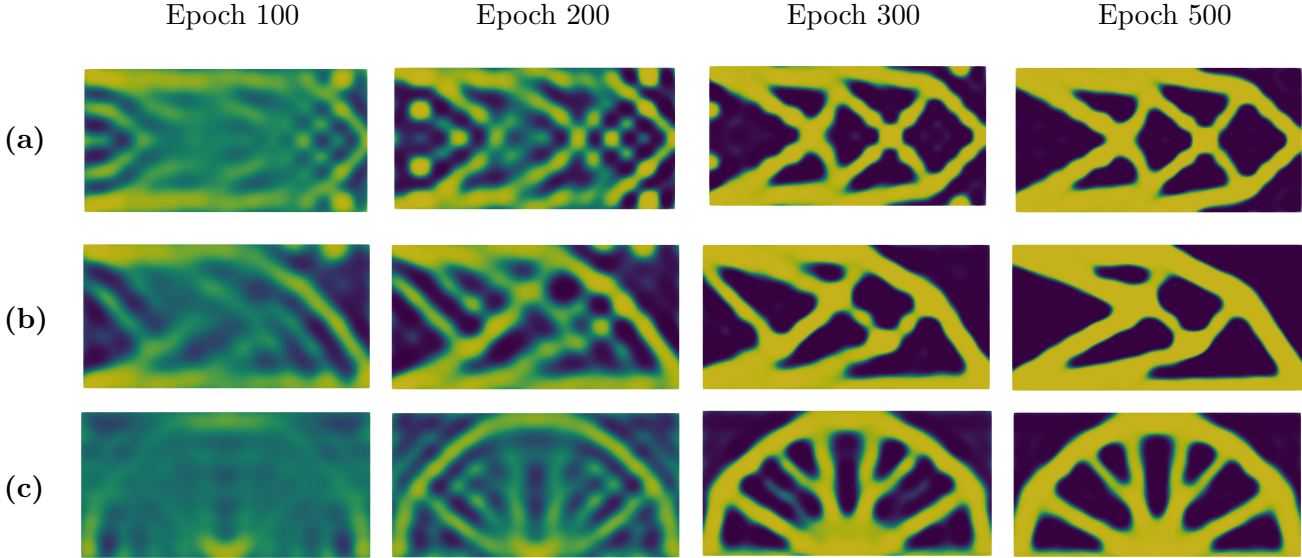


Figure 5: Topological evolution for the 2D compliance minimization benchmarks. Each row illustrates the progression from a diffuse, ambiguous initial state (left) to a crisp, well-defined final topology (right) for the (a) Cantilever, (b) Offset-loaded and (c) MBB beam cases, respectively.

The numerical results for the three 2D compliance minimization benchmarks are summarized in Figs. 5-6. Fig. 5 illustrates the topological evolution from a uniform initial phase-field of 0.5. The process transforms an initially diffuse and ambiguous material layout into distinct and well-defined truss-like structures. Crucially, the final designs are in excellent agreement with established benchmark solutions, confirming that the framework successfully navigates the design space to find physically rational topologies. This highlights a key advantage of the proposed method: it achieves high-quality final designs without the computational expense of requiring high-precision PDE solves at every intermediate iteration. Furthermore, the convergence history in Fig. 6 demonstrates the stability of the optimization, showing a monotonic decrease in compliance alongside effective enforcement of the volume constraint, indicating robust convergence to a

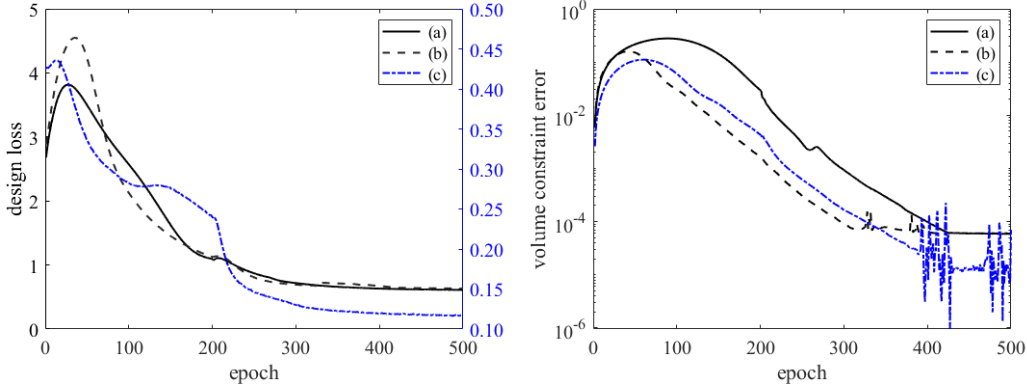


Figure 6: Convergence history for the 2D compliance minimization benchmarks, showing the design loss (left) and volume constraint error (right).

constrained optimum.

4.1.2 Compliance minimization in three dimensions

To further assess the framework’s performance in higher dimensions, it is validated on three distinct 3D compliance minimization benchmarks. All test cases are defined on a common computational domain $\Omega = (-1, 1) \times (-0.5, 0.5) \times (-0.2, 0.2)$ with boundary configurations specified as follows.

- (d) **3D Cantilever beam:** A standard cantilever setup. The left face $\Gamma_D = \{-1\} \times (-0.5, 0.5) \times (-0.2, 0.2)$ of the domain is clamped, and a downward traction of $\mathbf{t} = (0, -1, 0)^T$ is applied to a central patch on the right face $\Gamma_N = \{1\} \times (-0.05, 0.05) \times (-0.05, 0.05)$.
- (e) **3D Offset-loaded beam:** The cantilever setup is modified by relocating the load to the bottom-right corner of the structure. The traction is applied to the segment $\Gamma_N = \{1\} \times (-0.5, -0.4) \times (-0.05, 0.05)$ while the left face remains clamped.
- (f) **3D MBB beam:** The structure is supported at two regions on the bottom face $\Gamma_D = ((-1, -0.9) \cup (0.9, 1)) \times \{-0.5\} \times (-0.05, 0.05)$ and subjected to a downward traction on a central segment of the top face $\Gamma_N = (-0.05, 0.05) \times \{0.5\} \times (-0.05, 0.05)$.

The network architectures and training scheme largely follow the framework established for the 2D cases, with necessary adaptations for the three-dimensional domain. The state network is modified to accept 3D coordinates and output a 3D displacement vector. Its architecture comprises a Fourier feature mapping layer (512 features, scale of 20) followed by four hidden layers, each with 64 sine-activated neurons. The topology is again represented by a single-hidden-layer implicit network for the phase-field ϕ_σ . The optimization process employs the Adam optimizer with a learning rate of 1×10^{-3} for the state network and 5×10^{-3} for the topology network. The computational domain is discretized using a grid of $60 \times 30 \times 30$ collocation points. Training begins with a 10,000-epoch pre-training phase for the state network, followed by a 500-epoch main optimization loop to find the optimal topology.

The final optimized topologies for the three 3D compliance minimization problems are presented in Fig. 7. The optimization process successfully transforms an initially uniform and diffuse phase-field into intricate, well-defined truss-like structures, each tailored to its specific loading and boundary conditions.

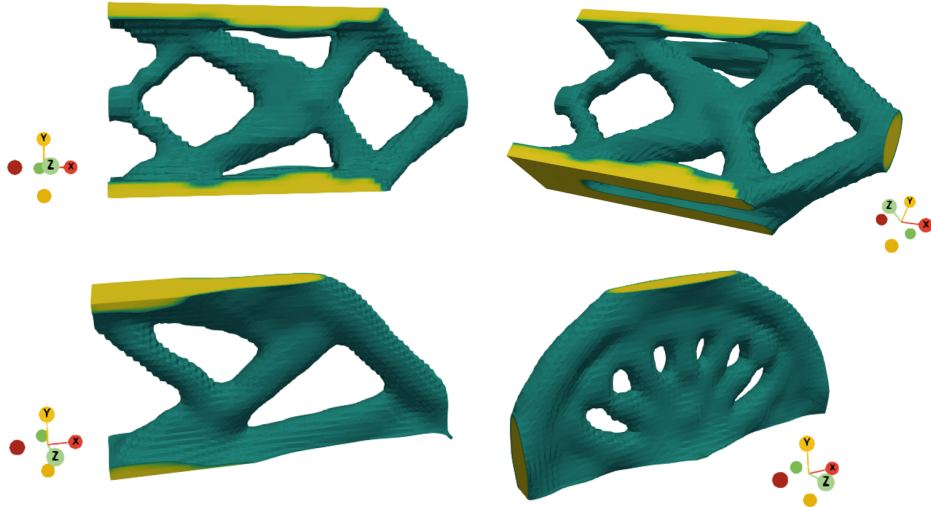


Figure 7: Final optimized topologies for the three 3D compliance minimization benchmarks. Top row: Two views of the 3D Cantilever beam. Bottom row: The final designs for the Offset-loaded beam (left) and the 3D MBB beam (right).

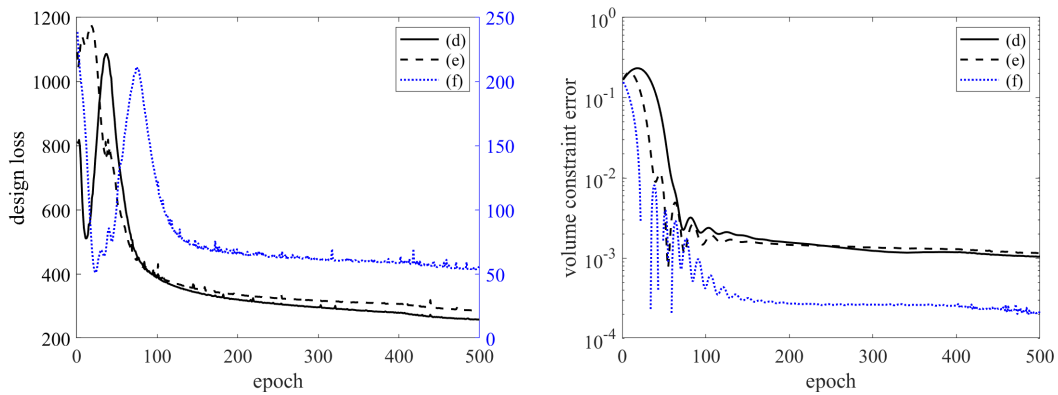


Figure 8: Convergence history for the 3D compliance minimization benchmarks, showing the design loss (left) and volume constraint error (right).

This evolutionary behavior mirrors the 2D benchmarks (cf. Fig. 5), confirming the robustness and consistency of the proposed method across dimensions. This robust performance is quantitatively substantiated by the convergence history in Fig. 8, which shows a stable and efficient optimization trajectory for all three cases.

4.2 Maximizing the first eigenvalue in linear elasticity

In contrast to compliance minimization, the gradient computation for eigenvalue maximization is remarkably straightforward. This simplification arises from the self-adjoint nature of the eigenvalue problem. Specifically, the first eigenvalue λ_1 is a stationary point of the Rayleigh quotient with respect to the eigenmode \mathbf{u}_θ . Consequently, its value is insensitive to first-order variations in the state field, meaning the implicit term involving the state field derivative $\frac{d\mathbf{u}_\theta}{d\phi_\sigma}$ vanishes.

For a mass-normalized eigenmode, where $\int_\Omega \varrho(\phi_\sigma) \|\mathbf{u}_\theta\|^2 d\mathbf{x} = 1$, the true physical sensitivity of λ_1 is given by

$$\frac{d\lambda_1}{d\phi_\sigma} = \int_\Omega \frac{\partial \mathbb{C}(\phi_\sigma)}{\partial \phi_\sigma} \boldsymbol{\varepsilon}(\mathbf{u}_\theta) : \boldsymbol{\varepsilon}(\mathbf{u}_\theta) d\mathbf{x} - \lambda_1 \int_\Omega \frac{\partial \varrho(\phi_\sigma)}{\partial \phi_\sigma} \|\mathbf{u}_\theta\|^2 d\mathbf{x}. \quad (4.6)$$

Crucially, due to the stationary property, this total derivative is identical to the partial derivative

$$\frac{d\lambda_1}{d\phi_\sigma} = \frac{\partial \lambda_1}{\partial \phi_\sigma}. \quad (4.7)$$

This identity has a powerful practical implication: the gradient computed by a standard AD framework on the Rayleigh quotient term is the true physical sensitivity. This allows for a direct application of AD without custom modifications, simplifying the implementation and guaranteeing that design updates correctly follow the path of steepest ascent.

4.2.1 Maximizing the first eigenvalue in two dimensions

The performance in 2D eigenvalue maximization is validated on two benchmarks, illustrated schematically in Fig. 9. Both cases use the same isotropic linear elastic material properties as the compliance problems. The specific setups are

- (g) **Partially constrained beam:** This case is defined in $\Omega = (-1, 1) \times (-0.5, 0.5)$. The structure is clamped on the entire left boundary and on a central segment of the right boundary, with the Dirichlet conditions defined by $\Gamma_D = \{-1\} \times (-0.5, 0.5) \cup \{1\} \times (-0.05, 0.05)$. All other boundaries are traction-free.
- (h) **Fully clamped beam:** This benchmark is computed in $\Omega = (-1, 1) \times (-0.25, 0.25)$. The vertical boundaries at $\mathbf{x}_1 = \pm 1$ are fully clamped, while the horizontal boundaries at $\mathbf{x}_2 = \pm 0.25$ are traction-free.

The setup for the eigenvalue maximization problems is adapted from the compliance cases with several key adjustments. The physical and penalty parameters are specifically tuned: the mass normalization constraint is weighted by $\lambda_{\text{norm}} = 50$, while the volume constraint penalty is handled with dynamic schemes. For the partially constrained case, the penalty starts at 1.0 and is amplified by 1.02 each epoch; for the fully clamped case, it starts at 10.0 and is amplified by 1.01. Architecturally, the state network is constructed with two hidden layers of 32 sine-activated neurons. The design network uses a single hidden layer with a deterministic frequency grid initialization up to a value of 25. Dirichlet boundary conditions are enforced by construction using different strategies:

- Case (g): A $\tanh(100(\mathbf{x}_1 + 1))$ term is used for the left boundary, supplemented by a soft penalty (weight 200, over 1000 points) for the right segment.
- Case (h): A composite term $\tanh(100(\mathbf{x}_1 + 1)) \cdot \tanh(100(1 - \mathbf{x}_1))$ is employed to enforce the clamped conditions on both vertical boundaries simultaneously.

The training procedure spans $N = 500$ epochs, with $K = 20$ state updates per epoch. The number of design updates M is scheduled to be 1 for the first 100 epochs and 5 thereafter. The state network is first pre-trained with a learning rate of 0.05 until its relative loss change falls below 10^{-5} (minimum 1000 iterations). For the main optimization, the learning rates are set to 10^{-4} for the state network and 5×10^{-4} for the topology network.



Figure 9: Problem setups for the two 2D eigenvalue maximization benchmarks: (g) the partially constrained beam and (h) the fully clamped beam.

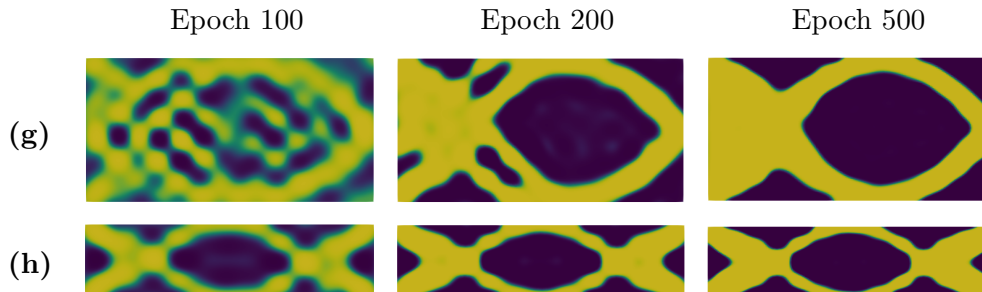


Figure 10: Evolution of the phase-field topology for the 2D eigenvalue maximization benchmarks, shown at different training epochs. Top row: Partially constrained beam. Bottom row: Fully clamped beam.

The results for 2D eigenvalue maximization in Figs. 10 and 11 demonstrate a robust and stable optimization process. Fig. 10 illustrates the evolutionary pathway from a diffuse initial state to a crisp and artifact-free final topology, culminating in physically optimal designs: a truss-stiffened frame for the partially constrained case and a classic spindle-like beam for the fully clamped case. The success of this process is quantitatively confirmed by the convergence plots in Fig. 11. The steady and monotonic decrease in the design loss, coupled with the effective enforcement of the volume constraint, provides clear evidence of a stable convergence towards a higher fundamental frequency.

4.2.2 Maximizing the first eigenvalue in three dimensions

To validate the framework’s scalability to 3D, we consider two eigenvalue maximization benchmarks that are direct three-dimensional extensions of the 2D cases. The problem setups are as follows. In both configurations, all boundaries not subject to Dirichlet conditions are specified as traction-free.

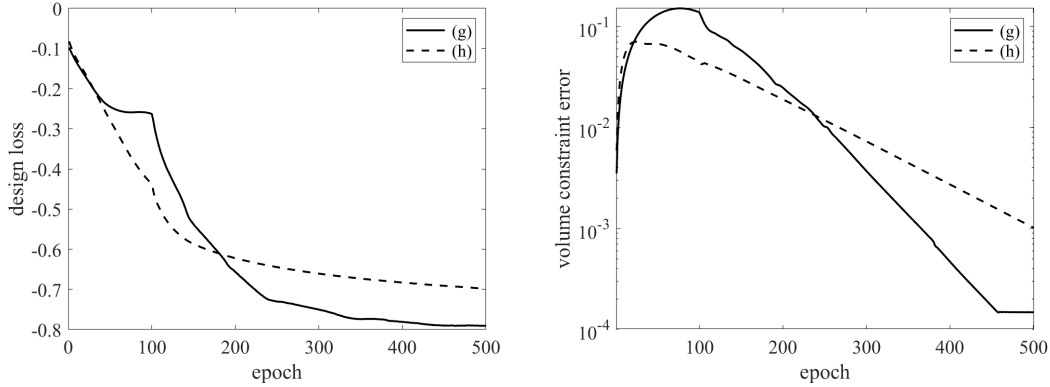


Figure 11: Convergence history for the 2D eigenvalue maximization benchmarks, showing the design loss (left) and volume constraint error (right) over 500 training epochs for the partially constrained (solid) and fully clamped (dashed) cases.

- (i) Extending the first 2D benchmark, this case uses a domain of $\Omega = (-1, 1) \times (-0.5, 0.5) \times (-0.2, 0.2)$. The structure is clamped on the entire left face and on a central segment of the right face, with the Dirichlet boundary defined as $\Gamma_D = \{-1\} \times (-0.5, 0.5) \times (-0.2, 0.2) \cup \{1\} \times (-0.05, 0.05) \times (-0.2, 0.2)$.
- (j) Analogous to the second 2D benchmark, this case involves a domain of $\Omega = (-1, 1) \times (-0.25, 0.25) \times (-0.3, 0.3)$. The vertical faces at $\mathbf{x}_1 = \pm 1$ are fully clamped, providing fixed supports at both ends.

The network architectures for the 3D cases consist of a state network with two hidden layers of 64 sine-activated neurons to approximate the eigenmode, and a design network with a single hidden layer initialized from a deterministic frequency grid (up to 25). Dirichlet boundary conditions are enforced by construction, using the same strategy as the 2D benchmarks. The training protocol begins with an extensive 5000-epoch pre-training of the state network (learning rate 0.005). This is followed by a 600-epoch main optimization loop, where the state and design networks are updated 100 times and 1 time per epoch, respectively. The learning rates for this main phase are 10^{-4} for the state network and 5×10^{-4} for the design network. The optimization is guided by two constraints. A mass normalization constraint is applied with a weight of $\lambda_{\text{norm}} = 50$. The volume constraint is managed by a dynamic penalty that starts at 100 and is amplified by 1.01 each epoch until it reaches a cap of 1000. Finally, the computational domains are discretized with uniform grids of $60 \times 30 \times 30$ for the first case and $80 \times 20 \times 20$ for the second.

The 3D eigenvalue maximization results in Figs. 12 and 13 further confirm the framework’s effectiveness. The final topologies are physically sound and artifact-free, yielding an asymmetric cantilever and a symmetric bridge-like structure, respectively. This high-quality outcome is supported by the convergence curves consistent with prior cases, which show stable loss reduction and effective constraint enforcement.

4.3 Stokes flow optimization

The optimization strategy for Stokes flow is greatly simplified by the problem’s inherent variational structure. Specifically, the governing Stokes equations are the Euler-Lagrange equations of the total energy functional \mathcal{J}_{obj} . A direct consequence of this formulation is that for a converged state field \mathbf{u}_θ satisfying the governing equations, the functional derivative of the objective with respect to the state variables vanishes identically.

$$\frac{\delta \mathcal{J}_{\text{obj}}}{\delta \mathbf{u}_\theta} = -\mu \Delta \mathbf{u}_\theta + \nabla p_\theta + \Pi(\phi_\sigma) \mathbf{u}_\theta - \mathbf{f} = 0. \quad (4.8)$$

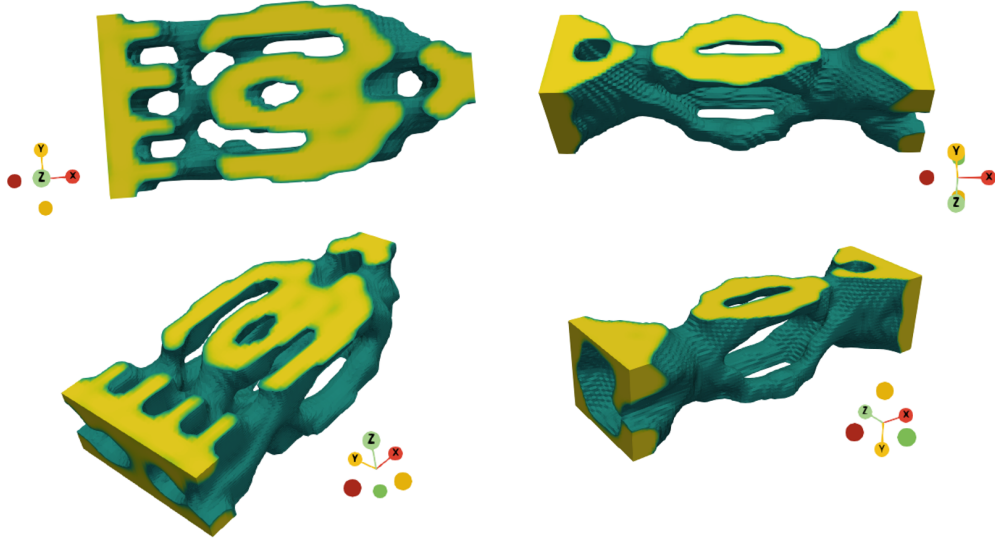


Figure 12: The evolution of phase-field function for eigenvalue maximization in 3D. 1st column: two different views of case (i); 2nd column: two different views of case (j).

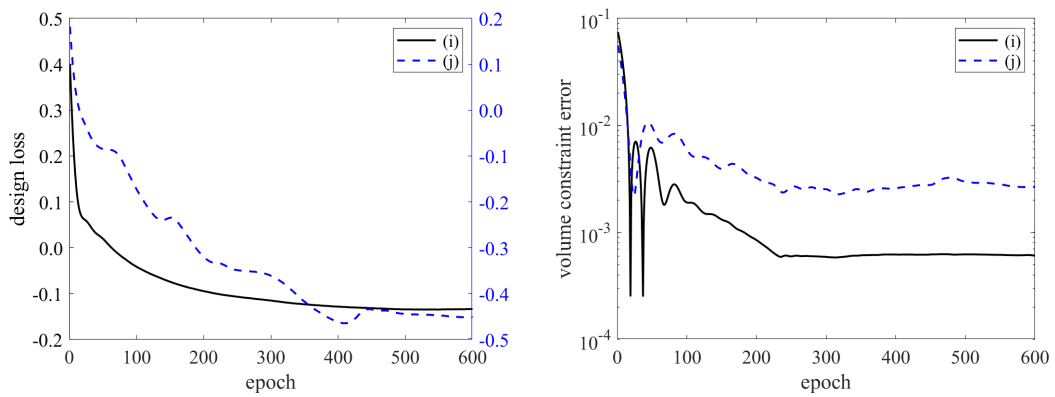


Figure 13: The convergence history of design loss function and volume constraint for eigenvalue maximization in 3D.

This property is crucial when evaluating the true design sensitivity. The total derivative of \mathcal{J}_{obj} with respect to the design field ϕ_{σ} must account for the implicit dependence of the state field \mathbf{u}_{θ} on the design. Applying the chain rule decomposes this total derivative into explicit and implicit components.

$$\frac{d\mathcal{J}_{\text{obj}}}{d\phi_{\sigma}} = \frac{\partial\mathcal{J}_{\text{obj}}}{\partial\phi_{\sigma}} + \left\langle \frac{\delta\mathcal{J}_{\text{obj}}}{\delta\mathbf{u}_{\theta}}, \frac{d\mathbf{u}_{\theta}}{d\phi_{\sigma}} \right\rangle. \quad (4.9)$$

Crucially, because the state field \mathbf{u}_{θ} is a solution to the governing equations, the sensitivity term $\frac{\delta\mathcal{J}_{\text{obj}}}{\delta\mathbf{u}_{\theta}}$ in the inner product is zero. This leads to a remarkable simplification where the entire implicit term vanishes.

This results in the following identity, which is of central importance to our optimization strategy.

$$\frac{d\mathcal{J}_{\text{obj}}}{d\phi_{\sigma}} = \frac{\partial\mathcal{J}_{\text{obj}}}{\partial\phi_{\sigma}}. \quad (4.10)$$

Eq. (4.10) demonstrates that the gradient computed via AD is equivalent to the true total design sensitivity. This direct correspondence, rooted in the variational nature of the power dissipation problem, allows us to use the raw gradient from the AD framework without modification. This obviates the need for custom gradient implementations, significantly streamlining the optimization process for Stokes flow.

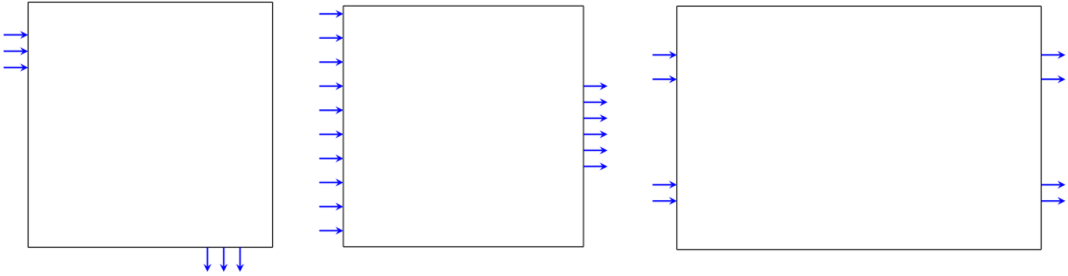


Figure 14: Schematic of the boundary conditions for the three 2D Stokes flow test cases, shown from left to right for cases (k), (l), and (m). Inward-pointing arrows denote prescribed velocity inflows (non-homogeneous Dirichlet), while outward-pointing arrows indicate zero-traction outflows (homogeneous Neumann). All unmarked boundaries are no-slip walls (homogeneous Dirichlet).

4.3.1 Stokes flow in two dimensions

The proposed framework is validated on the following three test cases in 2D, as shown in Fig. 14.

- (k) This case is simulated on the unit square $\Omega = (0, 1)^2$. A uniform inflow condition, $\mathbf{u}_{\theta} = (1, 0)^T$, is prescribed on the vertical segment $\mathbf{x}_1 = 0$ and $0.7 \leq \mathbf{x}_2 \leq 0.9$. A homogeneous Neumann condition is applied at the outflow port on the horizontal segment $\mathbf{x}_2 = 0$ and $0.7 \leq \mathbf{x}_1 \leq 0.9$. All other boundaries are treated as no-slip walls, i.e., $\mathbf{u}_{\theta} = \mathbf{0}$.
- (l) Within the unit square domain $\Omega = (0, 1)^2$, a parabolic inflow profile, $\mathbf{u}_{\theta} = (4\mathbf{x}_2(1 - \mathbf{x}_2), 0)^T$, is imposed on the left boundary $\mathbf{x}_1 = 0$. A zero Neumann outflow condition is set on the right boundary segment $\mathbf{x}_1 = 1$ and $0.3 \leq \mathbf{x}_2 \leq 0.7$. The remaining boundary edges are no-slip walls.
- (m) The problem is defined on a rectangular domain $\Omega = (0, 1.5) \times (0, 1)$ and is fully governed by Dirichlet conditions. On both the left $\mathbf{x}_1 = 0$ and right $\mathbf{x}_1 = 1.5$ boundaries, two symmetric parabolic velocity profiles are specified. The lower ports $1/6 \leq \mathbf{x}_2 \leq 1/3$ are subject to the profile $\mathbf{u}_{\theta} = (1 - 144(\mathbf{x}_2 -$

$1/4)^2, 0)^T$, while the upper ports $2/3 \leq \mathbf{x}_2 \leq 5/6$ are governed by $\mathbf{u}_\theta = (1 - 144(\mathbf{x}_2 - 3/4)^2, 0)^T$. A no-slip condition $\mathbf{u}_\theta = \mathbf{0}$ is enforced on all other boundary segments.

The velocity and pressure fields $(\mathbf{u}_\theta, p_\theta)$ are parameterized by a state network, which consists of four hidden layers with 64 neurons each and sinusoidal activation functions. To effectively capture complex flow patterns, this network first lifts the 2D spatial coordinates to a 512-dimensional feature space via a Gaussian random Fourier feature mapping layer. The topology is defined by the phase-field variable ϕ_σ , which is modeled by a second network. This topology network is an implicit neural representation with a single hidden layer that employs trainable frequency kernels to represent the material distribution. For all test cases, the fluid viscosity is consistently set to $\mu = 0.01$.

The training procedure begins with a 10,000-epoch pre-training of the state network to establish a stable initial flow field. Subsequently, the main optimization loop is run for 400 epochs for case (k) and 500 epochs for cases (l) and (m). Both networks are trained using the Adam optimizer, with learning rates of 1×10^{-3} and 5×10^{-3} for the state and topology networks, respectively. The state network’s loss function is a weighted sum of the governing PDE residuals and boundary condition terms; the weight for the boundary loss is set to 10.0 for cases (k)-(l) and increased to 20.0 for case (m). Several key hyperparameters are tailored for each case. The target volume fractions β are 0.3 for case (k) and 0.5 for cases (l) and (m). The number of domain and boundary collocation points are (20,000, 5,000) for cases (k)-(l) and increased to (30,000, 8,000) for the larger domain in case (m). Finally, the Darcy penalization parameter η , which enforces the solid phase, is set to 50 (k), 100 (l) and 50 (m), respectively, to ensure robust optimization.

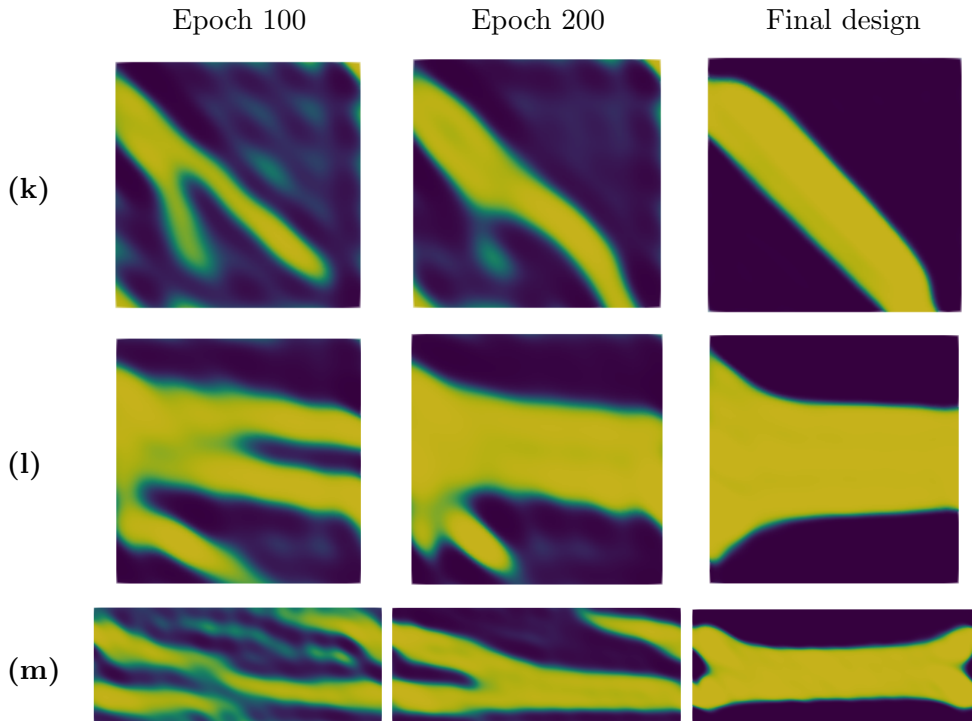


Figure 15: Evolution of the phase field for Stokes flow test cases (k-m) in 2D at selected training epochs.

The effectiveness and robust performance are demonstrated in Figs. 15 and 16. Fig. 15 shows the phase-field evolution from an initial diffuse state to a final crisp topology, successfully forming well-defined structures. The corresponding convergence history in Fig. 16 confirms the stability of this process, exhibit-

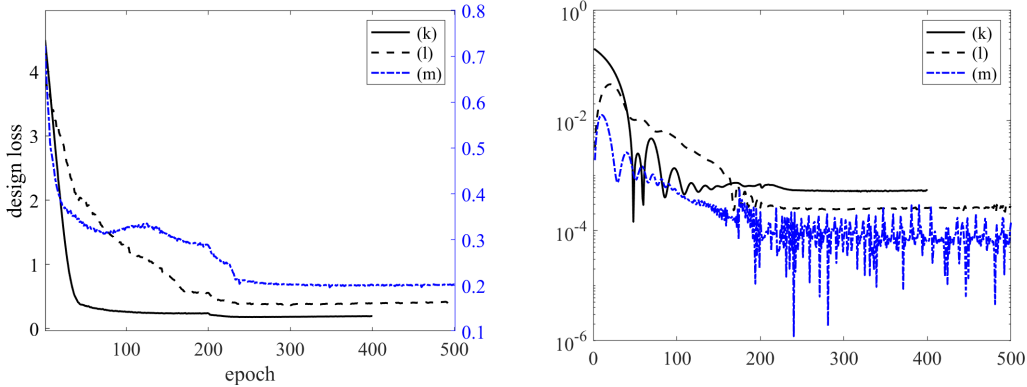


Figure 16: Training history for the 2D Stokes flow test cases, illustrating the convergence of the design loss (left) and the volume constraint error (right, log scale). Note that the design loss for case (m) is plotted against the right-hand y-axis.

ing a monotonic decrease in the design loss while the volume constraint is effectively satisfied throughout the optimization.

4.3.2 Stokes flow in three dimensions

The framework is also validated on two 3D Stokes flow problems designed to minimize power dissipation.

- (n) This problem is defined on the unit cube $\Omega = (0, 1)^3$. Four circular inlets are located on the side faces ($\mathbf{x}_1 = 0, 1$ and $\mathbf{x}_2 = 0, 1$) with inflow velocities of $(1, 0, 0)^T$, $(-1, 0, 0)^T$, $(0, 1, 0)^T$, and $(0, -1, 0)^T$, respectively. To ensure mass conservation, a single circular outlet on the bottom face ($\mathbf{x}_3 = 0$) is prescribed with a velocity of $(0, 0, -4)^T$. All other boundaries are no-slip walls ($\mathbf{u}_\theta = \mathbf{0}$).
- (o) Also defined on the unit cube, this case features a uniform inflow of $\mathbf{u} = (0, 1, 0)^T$ across the entire bottom face ($\mathbf{x}_2 = 0$). A mass-conserving parabolic velocity profile is enforced at a circular outlet centered on the top face ($\mathbf{x}_2 = 1$). The remaining boundaries are no-slip walls.

The network architectures and learning rates are consistent for both 3D problems. The state network uses a Fourier feature mapping layer (256 features, scale 10) followed by four hidden layers of 128 sine-activated neurons. The design network is a single-layer implicit neural representation with frequency kernels initialized up to 15. Learning rates are fixed at 1×10^{-3} for the state network and 5×10^{-3} for the design network. The remaining training and physical parameters are tailored to each case. For case (n), the state network is pre-trained for 10,000 epochs, followed by a 700-epoch main optimization. The Darcy penalization η is 50, and the target volume fraction β is 0.25. For case (o), these are adjusted to 5,000 pre-training epochs, 1,000 main optimization epochs, $\eta = 100$, and $\beta = 0.4$. The 3D results, presented in Figs. 17 and 18, confirm the framework’s robust scalability. The optimization yields high-quality topologies for both the multi-inlet mixer (n) and the diffuser (o), while the training process exhibits the same stable convergence behavior observed in the 2D cases.

4.4 Navier-Stokes flow optimization

The optimization of Navier-Stokes flow is fundamentally different from the Stokes case due to the non-variational nature of the convective term $(\mathbf{u} \cdot \nabla)\mathbf{u}$. This breaks the direct correspondence between the governing equations and the Euler-Lagrange equations of the power dissipation objective \mathcal{J}_{obj} .

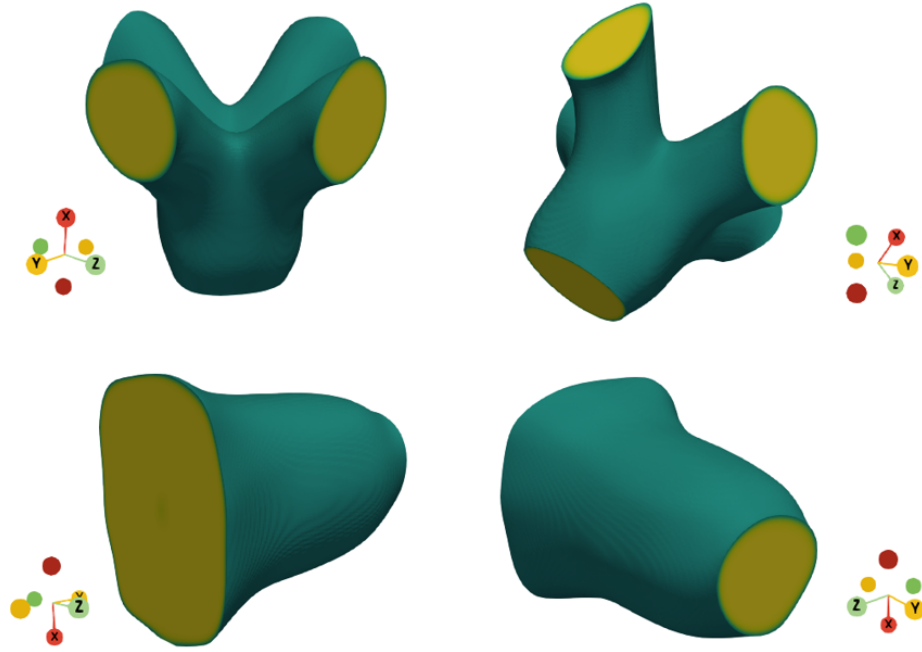


Figure 17: Final optimized topologies for the 3D Stokes flow problems. The top row presents two perspective views of the case (n). The bottom row displays two views of the final design for the case (o).

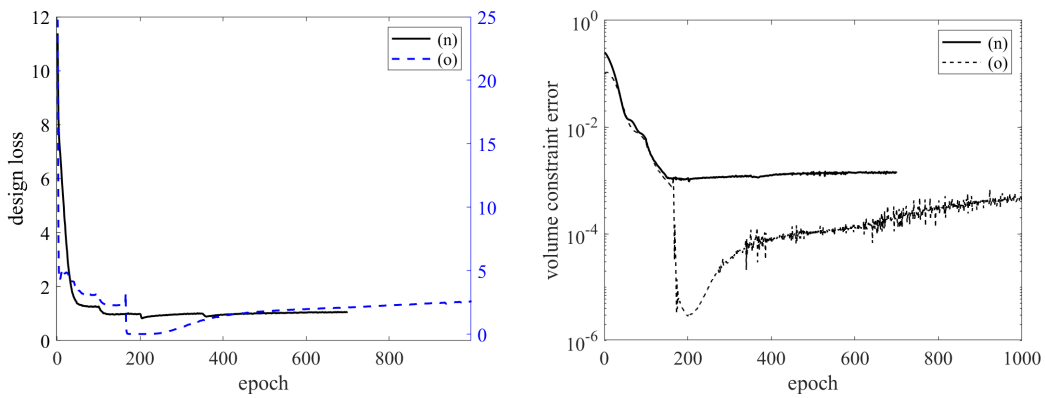


Figure 18: Convergence history for the 3D Stokes flow optimization. (Left) Design loss versus epoch, where the curve for the case (o) is plotted against the secondary y-axis on the right. (Right) Volume constraint error on a logarithmic scale.

Specifically, for a converged state where the Navier-Stokes residual $\mathbf{R}_{\text{NS}} = 0$, the functional derivative of the objective no longer vanishes. Instead, it becomes equal to the negative of the convective term

$$\frac{\delta \mathcal{J}_{\text{obj}}}{\delta \mathbf{u}_{\theta}} = -(\mathbf{u}_{\theta} \cdot \nabla) \mathbf{u}_{\theta} \neq 0. \quad (4.11)$$

Consequently, the chain rule for the total design derivative contains a non-vanishing implicit term

$$\frac{d \mathcal{J}_{\text{obj}}}{d \phi_{\sigma}} = \frac{\partial \mathcal{J}_{\text{obj}}}{\partial \phi_{\sigma}} - \left\langle (\mathbf{u}_{\theta} \cdot \nabla) \mathbf{u}_{\theta}, \frac{d \mathbf{u}_{\theta}}{d \phi_{\sigma}} \right\rangle. \quad (4.12)$$

This means the gradient computed by AD $\frac{\partial \mathcal{J}_{\text{obj}}}{\partial \phi_{\sigma}}$ is incomplete. The adjoint method is therefore introduced to efficiently compute the additional inner product term. To obtain the true design sensitivity, the alternating scheme shown in Algorithm 1 is necessarily augmented with an adjoint solver.

Specifically, given $\Pi(\phi_{\sigma}) = \eta(1 - \phi_{\sigma})^2$, the sensitivity of the physical objective is explicitly computed as [27]

$$\frac{d \mathcal{J}_{\text{obj}}}{d \phi_{\sigma}} = \frac{\partial \Pi}{\partial \phi_{\sigma}} \left(\frac{1}{2} |\mathbf{u}_{\theta}|^2 - \mathbf{w}_{\alpha} \cdot \mathbf{u}_{\theta} \right) = -2\eta(1 - \phi_{\sigma}) \left(\frac{1}{2} |\mathbf{u}_{\theta}|^2 - \mathbf{w}_{\alpha} \cdot \mathbf{u}_{\theta} \right). \quad (4.13)$$

Therefore, the complete gradient for the total topology loss function $\mathcal{L}_{\text{topology}}$, which is used for the back-propagation step to update the topology network parameters σ , is constructed by combining this physically rigorous sensitivity with the straightforward derivatives of the regularization terms

$$\nabla_{\sigma} \mathcal{L}_{\text{topology}} = \left\langle \frac{d \mathcal{J}_{\text{obj}}}{d \phi_{\sigma}} + \frac{\delta \mathcal{E}_{\text{GL}}}{\delta \phi_{\sigma}} + \frac{\delta \mathcal{P}_{\text{vol}}}{\delta \phi_{\sigma}}, \frac{\partial \phi_{\sigma}}{\partial \sigma} \right\rangle, \quad (4.14)$$

where $\delta \mathcal{E}_{\text{GL}}/\delta \phi_{\sigma}$ and $\delta \mathcal{P}_{\text{vol}}/\delta \phi_{\sigma}$ are the variational derivatives of the Ginzburg-Landau energy and the volume constraint penalty, respectively, and are computed directly via AD. This formulation ensures that the design update is guided by the true total gradient, which is essential for the stability and convergence of the optimization for non-self-adjoint systems.

The performance of the framework on non-self-adjoint problems is validated on a series of 2D and 3D Navier-Stokes flow optimizations.

- (p) Defined on a unit square, this case features a parabolic inflow profile $\mathbf{u}_{\theta} = (1 - 100(\mathbf{x}_2 - 0.5)^2, 0)^{\text{T}}$ on the inlet segment $\mathbf{x}_1 = 0$ and $0.7 \leq \mathbf{x}_2 \leq 0.9$. The outlet at $\mathbf{x}_2 = 0$ and $0.7 \leq \mathbf{x}_1 \leq 0.9$ has a prescribed profile of $\mathbf{u}_{\theta} = (0, 100(\mathbf{x}_1 - 0.5)^2 - 1)^{\text{T}}$. All other boundaries are no-slip walls.
- (q) On a unit square domain, a parabolic inflow $\mathbf{u}_{\theta} = (1 - 4(\mathbf{x}_2 - 0.5)^2, 0)$ is imposed on the left boundary $\mathbf{x}_1 = 0$. The outlet on the right boundary has a specified profile $\mathbf{u}_{\theta} = (3 - 108(\mathbf{x}_2 - 0.5)^2, 0)$ on the segment $1/3 \leq \mathbf{x}_2 \leq 2/3$. The top and bottom boundaries are no-slip walls.
- (r) This case features two parabolic inlets on the left boundary $\mathbf{x}_1 = 0$ of a unit square:
 - Upper inlet ($2/3 \leq \mathbf{x}_2 \leq 5/6$): $\mathbf{u}_{\theta} = (1 - 144(\mathbf{x}_2 - 0.75)^2, 0)$.
 - Lower inlet ($1/6 \leq \mathbf{x}_2 \leq 1/3$): $\mathbf{u}_{\theta} = (1 - 144(\mathbf{x}_2 - 0.25)^2, 0)$.

The fluid exits through the right boundary under a zero-traction condition, while the top and bottom boundaries are no-slip walls.

- (s) The setup for this 3D case is identical to the Stokes flow mixer described in case (o).

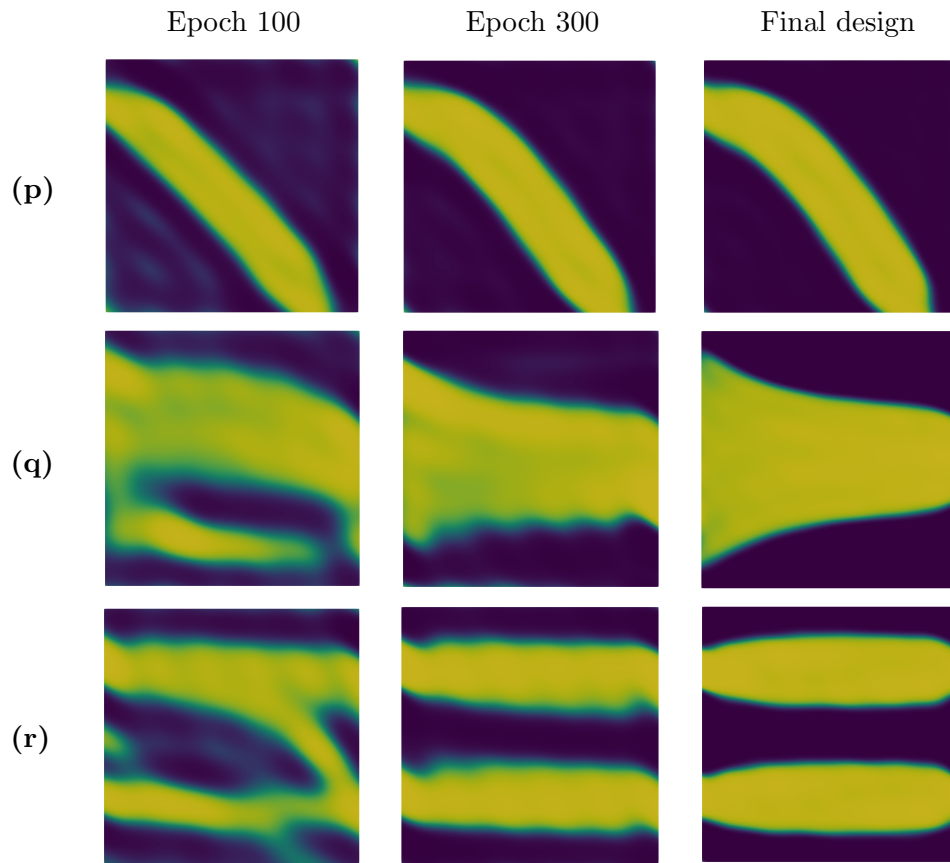


Figure 19: Topological evolution for the 2D Navier-Stokes test cases (p)-(r).

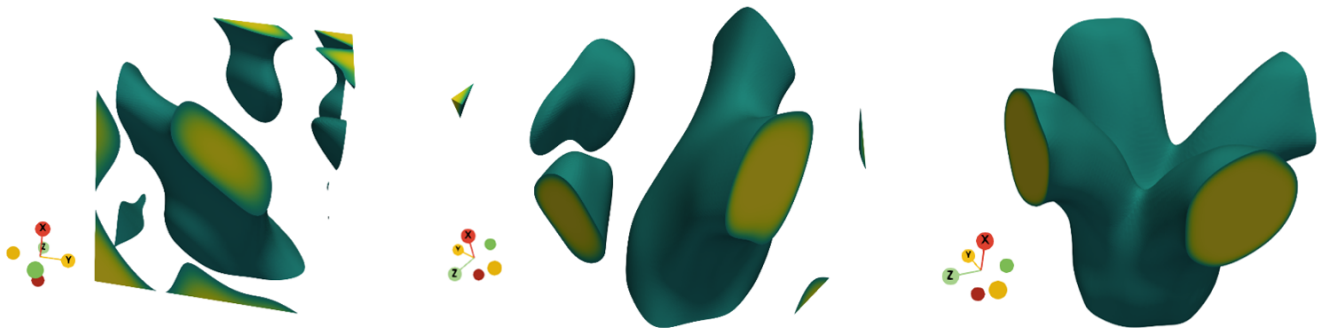


Figure 20: Evolution of the phase-field topology for the 3D Navier-Stokes case (s) at epochs 100, 200 and 1000 from left to right.

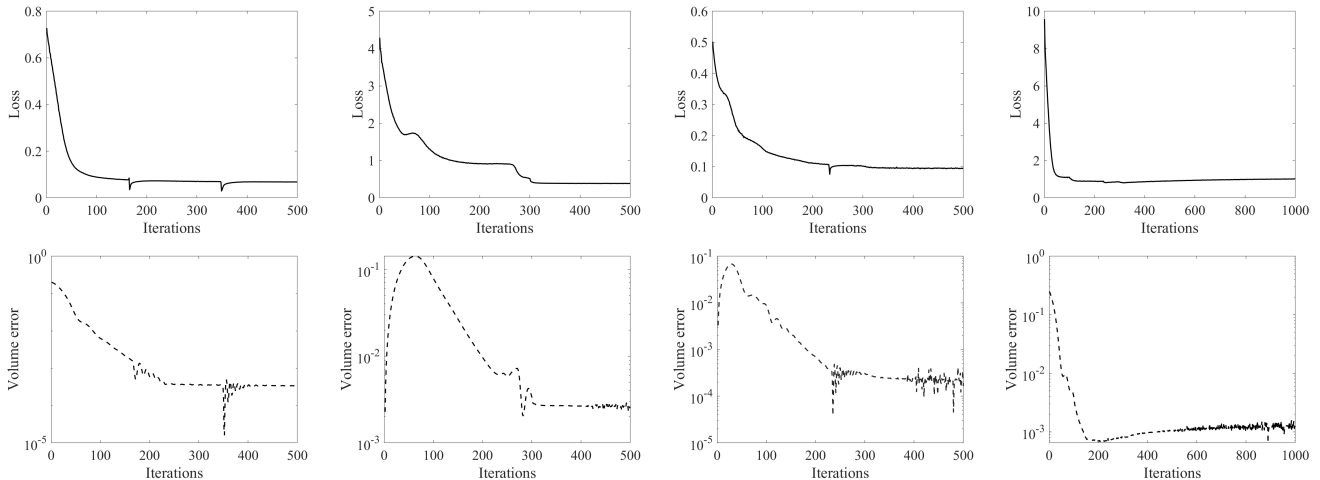


Figure 21: Training history for the Navier-Stokes test cases (p)-(s), shown column-wise. For each case, the top plot shows the design loss, and the bottom plot shows the volume constraint error (log scale).

The final set of experiments validates the framework’s efficacy on challenging Navier-Stokes problems, where the adjoint-augmented scheme is essential for computing the correct design sensitivity. The results, summarized in Figs. 19–21, demonstrate that this approach successfully produces well-resolved and physically meaningful topologies for both 2D and 3D cases. Notably, the framework’s flexibility is highlighted in the 3D design (Fig. 20), which required navigating a significant topological change to merge several initially disconnected regions into a single, complex manifold. The convergence histories for all cases in Fig. 21 confirm that this robust performance is underpinned by a stable training process, consistent with the self-adjoint examples. Collectively, these results validate that the proposed adjoint-based framework is a stable and highly effective method for optimizing non-self-adjoint problems.

5 Conclusion

The proposed APF-FNN presents a unified and physics-driven framework for phase-field topology optimization, capable of generating high-resolution and high-performance designs for both self-adjoint and non-self-adjoint systems. At its core, the APF-FNN employs a stable alternating training scheme that decouples the optimization problem by parameterizing the state, adjoint, and phase-field variables with three independent Fourier Neural Networks. This architecture provides a flexible foundation for solving diverse physics-based design problems. A distinctive feature of the framework is its topology network update strategy, which integrates sensitivity analysis with automatic differentiation to guide the design along the most efficient optimization path. Incorporating the Ginzburg–Landau energy functional into the loss function further serves as a physical regularizer, promoting sharp, smooth and well-defined two-phase structures. Unlike traditional approaches that evolve gradient flow equations in pseudo-time, the APF-FNN directly computes the steady-state phase-field satisfying first-order optimality conditions. Extensive 2D and 3D benchmarks confirm its robustness and versatility, highlighting its potential to advance computational design. This framework also offers a promising foundation for future extensions to coupled multiphysics problems and complex engineering domains.

Acknowledgments

This work is supported in part by the National Key Basic Research Program under Grant 2022YFA1004402, the National Natural Science Foundation of China under Grant (No.12471377), and the Science and Technology Commission of Shanghai Municipality (Nos. 23JC1400503 and 22DZ2229014).

References

- [1] M.P. Bendsøe and O. Sigmund. *Topology Optimization: Theory, Methods, and Applications*. Springer, 2003.
- [2] S. Zargham, T.A. Ward, R. Ramli, and I.A. Badruddin. Topology optimization: a review for structural designs under vibration problems. *Struct. Multidiscip. Optim.*, 53(6):1157–1177, 2016.
- [3] Allaire G., Dapogny C., and Jouve F. Chapter 1 - shape and topology optimization. In Andrea Bonito and Ricardo H. Nochetto, editors, *Geometric Partial Differential Equations - Part II*, volume 22 of *Handbook of Numerical Analysis*, pages 1–132. Elsevier, 2021.
- [4] O. Giraldo-Londoño, L. Mirabella, L. Dalloro, and G.H. Paulino. Multi-material thermomechanical topology optimization with applications to additive manufacturing: Design of main composite part and its support structure. *Comput. Methods Appl. Mech. Engrg.*, 363:112812, 2020.
- [5] Chen H., Dong P., Wang D., and Wang X. A prediction-correction based iterative convolution-thresholding method for topology optimization of heat transfer problems. *J. Comput. Phys.*, 511:113119, 2024.
- [6] A. Takezawa, A.C. To, Q. Chen, X. Liang, F. Dugast, X. Zhang, and M. Kitamura. Sensitivity analysis and lattice density optimization for sequential inherent strain method used in additive manufacturing process. *Comput. Methods Appl. Mech. Engrg.*, 370:113231, 2020.
- [7] Y. Luo, O. Sigmund, Q. Li, and S. Liu. Additive manufacturing oriented topology optimization of structures with self-supported enclosed voids. *Comput. Methods Appl. Mech. Engrg.*, 372:113385, 2020.
- [8] M.P. Bendsøe and N. Kikuchi. Generating optimal topologies in structural design using a homogenization method. *Comput. Methods Appl. Mech. Engrg.*, 71(2):197–224, 1988.
- [9] O. Sigmund and K. Maute. Topology optimization approaches: A comparative review. *Struct. Multidiscip. Optim.*, 48(6):1031–1055, 2013.
- [10] M.P. Bendsøe. Optimal shape design as a material distribution problem. *Struct. Optim.*, 1(4):193–202, 1989.
- [11] M.P. Bendsøe and O. Sigmund. Material interpolation schemes in topology optimization. *Arch. Appl. Mech.*, 69(9):635–654, 1999.
- [12] X. Huang and Y. Xie. Convergent and mesh-independent solutions for the bi-directional evolutionary structural optimization method. *Finite Elem. Anal. Des.*, 43(14):1039–1049, 2007.
- [13] A. Diaz and O. Sigmund. Checkerboard patterns in layout optimization. *Struct. Optim.*, 10(1):40–45, 1995.

- [14] O. Sigmund and J. Petersson. Numerical instabilities in topology optimization: a survey on procedures dealing with checkerboards, mesh-dependencies and local minima. *Struct. Optim.*, 16(1):68–75, 1998.
- [15] B. Bourdin. Filters in topology optimization. *Int. J. Numer. Meth. Eng.*, 50(9):2143–2158, 2001.
- [16] T.E. Bruns and D.A. Tortorelli. Topology optimization of non-linear elastic structures and compliant mechanisms. *Comput. Methods Appl. Mech. Engrg.*, 190(26-27):3443–3459, 2001.
- [17] J.A. Sethian and A. Wiegmann. Structural boundary design via level set and immersed interface methods. *J. Comput. Phys.*, 163(2):489–528, 2000.
- [18] M.Y. Wang, X. Wang, and D. Guo. A level set method for structural topology optimization. *Comput. Methods Appl. Mech. Engrg.*, 192(1-2):227–246, 2003.
- [19] X. Hu, M. Qian, and S. Zhu. Accelerating a phase field method by linearization for eigenfrequency topology optimization. *Struct. Multidiscip. Optim.*, 66(12):242, 2023.
- [20] M. Qian, X. Hu, and S. Zhu. A phase field method based on multi-level correction for eigenvalue topology optimization. *Comput. Methods Appl. Mech. Eng.*, 401:115646, 2022.
- [21] S. Wu, X. Hu, and S. Zhu. A multi-mesh finite element method for phase-field based photonic band structure optimization. *J. Comput. Phys.*, 357:324–337, 2018.
- [22] J. Li, H. Yang, and S. Zhu. Efficient multimodes Monte Carlo Method for structural topology optimization with random uncertainties. *Int. J. Numer. Methods Eng.*, 126(21):e70172, 2025.
- [23] M.Y. Wang and S. Zhou. Phase field: a variational method for structural topology optimization. *Comput. Model. Eng. Sci.*, 6(6):547, 2004.
- [24] B. Bourdin and A. Chambolle. Design-dependent loads in topology optimization. *ESAIM: Control Optim. Calc. Var.*, 9:19–48, 2003.
- [25] P.I. Plotnikov and J. Sokolowski. Geometric aspects of shape optimization. *The Journal of Geometric Analysis*, 33(7):206, 2023.
- [26] L.Q. Chen. Phase-field models for microstructure evolution. *Annu. Rev. Mater. Res.*, 32(1):113–140, 2002.
- [27] J. Li and S. Zhu. Energy stable gradient flow schemes for shape and topology optimization in Navier-Stokes flows. *Comm. Comput. Phys.*, 38:404–438, 2025.
- [28] B. Bourdin and A. Chambolle. The phase-field method in optimal design. In *IUTAM Symposium on Topological Design Optimization of Structures, Machines and Materials: Status and Perspectives*, pages 207–215. Springer, 2006.
- [29] C. Gogu. Improving the efficiency of large scale topology optimization through on-the-fly reduced order model construction. *Int. J. Numer. Methods Eng.*, 101(4):281–304, 2015.
- [30] O. Amir and O. Sigmund. On reducing computational effort in topology optimization: how far can we go? *Struct. Multidiscip. Optim.*, 44(1):25–29, 2011.
- [31] I.E. Lagaris, A. Likas, and D.I. Fotiadis. Artificial neural networks for solving ordinary and partial differential equations. *IEEE Trans. Neural Netw.*, 9(5):987–1000, 1998.

- [32] M. Raissi, P. Perdikaris, and G.E. Karniadakis. Physics-informed neural networks: A deep learning framework for solving forward and inverse problems involving nonlinear partial differential equations. *J. Comput. Phys.*, 378:686–707, 2019.
- [33] W. E and B. Yu. The deep Ritz method: A deep learning-based numerical algorithm for solving variational problems. *Commun. Math. Stat.*, 6(1):1–12, 2018.
- [34] G.E. Karniadakis, I.G. Kevrekidis, L. Lu, P. Perdikaris, S. Wang, and L. Yang. Physics-informed machine learning. *Nat. Rev. Phys.*, 3(6):422–440, 2021.
- [35] Z. Li, N. Kovachki, K. Azizzadenesheli, B. Liu, K. Bhattacharya, A. Stuart, and A. Anandkumar. Fourier neural operator for parametric partial differential equations. *arXiv preprint arXiv:2010.08895*, 2020.
- [36] S. Yu, Q. He, S. Zhang, and H. Gong. Tensor neural network combined with Nitsche method for solving interface problems. *J. Comput. Appl. Math.*, 475:117002, 2026.
- [37] S. Shin, D. Shin, and N. Kang. Topology optimization via machine learning and deep learning: a review. *J. Comput. Des. Eng.*, 10(4):1736–1766, 2023.
- [38] R.V. Woldseth, N. Aage, J. A. Bærentzen, and O. Sigmund. On the use of artificial neural networks in topology optimisation. *Struct. Multidiscip. Optim.*, 65(10):294, 2022.
- [39] I. Sosnovik and I. Oseledets. Neural networks for topology optimization. *Russ. J. Numer. Anal. Math. Model.*, 34(4):215–223, 2019.
- [40] S. Banga, H. Gehani, S. Bhilare, S. Patel, and L. Kara. 3d topology optimization using convolutional neural networks. *arXiv preprint arXiv:1808.07440*, 2018.
- [41] T. Sugai, K. Shintani, and T. Yamada. Data-driven topology optimization using a multitask conditional variational autoencoder with persistent homology. *Struct. Multidisc. Optim.*, 67(133), 2024.
- [42] Yamasaki S., Yaji K., and Fujita K. Data-driven topology design using a deep generative model. *Struct. Multidiscip. Optim.*, 64:1401–1420, 2021.
- [43] W. Hao, J. Du, Z. and Li, I. Slavashevich, and X. Guo. Machine learning enhanced multiscale topology optimization with structural genome databases. *Struct. Multidiscip. Optim.*, 64:1401–1420, 2021.
- [44] Z. Nie, T. Lin, H. Jiang, and L.B. Kara. Topologygan: Topology optimization using generative adversarial networks based on physical fields over the initial domain. *J. Mech. Des.*, 143(3):031715, 2021.
- [45] C.M. Parrott, D.W. Abueidda, and K.A. James. Multidisciplinary topology optimization using generative adversarial networks for physics-based design enhancement. *J. Mech. Des.*, 145(6):061704, 2023.
- [46] M. Greminger. Generative adversarial networks with synthetic training data for enforcing manufacturing constraints on topology optimization. In *ASME IDETC/CIE Conference*, volume 84003, page V11AT11A005. American Society of Mechanical Engineers, 2020.
- [47] A. Chandrasekhar and K. Suresh. TouNN: topology optimization using neural networks. *Struct. Multidiscip. Optim.*, 63(3):1135–1149, 2021.

- [48] S.M. Sanu, A.M. Aragón, and M.A. Bessa. Neural topology optimization: the good, the bad, and the ugly. *Struct. Multidiscip. Optim.*, 68(10):1–26, 2025.
- [49] H. Jeong, J. Bai, C.P. Batuwatta-Gamage, C. Rathnayaka, Y. Zhou, and Y. Gu. A physics-informed neural network-based topology optimization (PINNTO) framework for structural optimization. *Eng. Struct.*, 278:115484, 2023.
- [50] J. Zehnder, Y. Li, S. Coros, and B. Thomaszewski. Ntopo: Mesh-free topology optimization using implicit neural representations. *Adv. Neural Inf. Process. Syst.*, 34:10368–10381, 2021.
- [51] A. Singh, S. Chakraborty, and R. Chowdhury. A dual physics-informed neural network for topology optimization. *arXiv preprint arXiv:2410.14342*, 2024.
- [52] A. Joglekar, H. Chen, and L.B. Kara. DMF-TONN: direct mesh-free topology optimization using neural networks. *Eng. Comput.*, 40(4):2227–2240, 2024.
- [53] A. Yousefpour, S. Hosseinmardi, C. Mora, and R. Bostanabad. Simultaneous and meshfree topology optimization with physics-informed gaussian processes. *Comput. Methods Appl. Mech. Eng.*, 437:117698, 2025.
- [54] S. Lai, J. Feng, Z. Lv, J. Kim, and Y. Li. A dual-energy physics-informed multi-material topology optimization method within the phase-field framework. *Comput. Methods Appl. Mech. Eng.*, 447:118338, 2025.
- [55] H. Garcke and C. Hecht. Shape and topology optimization in Stokes flow with a phase field approach. *Appl. Math. Optim.*, 73(1):23–70, 2016.
- [56] L. Blank, H. Garcke, L. Sarbu, T. Srisupattarananit, V. Styles, and A. Voigt. Phase-field approaches to structural topology optimization. In *Constr. Optim. Optim. Control Partial Differ. Equ.*, pages 245–256. Springer, 2011.
- [57] B. Jin, J. Li, Y. Xu, and S. Zhu. An adaptive phase-field method for structural topology optimization. *J. Comput. Phys.*, 506:112932, 2024.
- [58] A. Takezawa, S. Nishiwaki, and M. Kitamura. Shape and topology optimization based on the phase field method and sensitivity analysis. *J. Comput. Phys.*, 229(7):2697–2718, 2010.
- [59] J. Li, Y. Xu, and S. Zhu. Adaptive computation of elliptic eigenvalue topology optimization with a phase-field approach. *J. Numer. Math.*, 2025.
- [60] M. Tancik, P. Srinivasan, B. Mildenhall, S. Fridovich-Keil, N. Raghavan, U. Singhal, R. Ramamoorthi, J. Barron, and R. Ng. Fourier features let networks learn high frequency functions in low dimensional domains. *Adv. Neural Inf. Process. Syst.*, 33:7537–7547, 2020.
- [61] B. Jin, J. Li, Y. Xu, and S. Zhu. On the Crouzeix-Raviart finite element approximation of phase-field dependent topology optimization in Stokes flow. *arXiv preprint arXiv:2505.04120, to appear, Int. J. Numer. Methods Eng.*, 2025.